



# Design of materials with prescribed nonlinear properties



F. Wang<sup>a,\*</sup>, O. Sigmund<sup>a</sup>, J.S. Jensen<sup>a,b</sup>

<sup>a</sup> Department of Mechanical Engineering, Technical University of Denmark, Nils Koppels Allé, Building 404, 2800 Kgs. Lyngby, Denmark

<sup>b</sup> Department of Electrical Engineering, Technical University of Denmark, Ørstedes Plads, Building 352, 2800 Kgs. Lyngby, Denmark

## ARTICLE INFO

### Article history:

Received 5 September 2013

Received in revised form

17 March 2014

Accepted 5 May 2014

Available online 14 May 2014

### Keywords:

Material design

Finite deformation

Nonlinear properties

Optimization

## ABSTRACT

We systematically design materials using topology optimization to achieve prescribed nonlinear properties under finite deformation. Instead of a formal homogenization procedure, a numerical experiment is proposed to evaluate the material performance in longitudinal and transverse tensile tests under finite deformation, i.e. stress–strain relations and Poisson's ratio. By minimizing errors between actual and prescribed properties, materials are tailored to achieve the target. Both two dimensional (2D) truss-based and continuum materials are designed with various prescribed nonlinear properties. The numerical examples illustrate optimized materials with rubber-like behavior and also optimized materials with extreme strain-independent Poisson's ratio for axial strain intervals of  $\epsilon_i \in [0.00, 0.30]$ .

© 2014 Elsevier Ltd. All rights reserved.

## 1. Introduction

Novel materials with special properties are highly attractive for modern technology. This comprises materials with exotic mechanical properties (Lakes, 1987; Evans, 1991; Safari, 1994) and materials with enhanced electric and magnetic properties (Scarpa and Smith, 2004; Shvets and Urzhumov, 2005). Materials with negative Poisson's ratio (NPR), known as auxetic materials, are one type of materials with unusual mechanical properties. In contrast to conventional materials, such materials will expand instead of shrinking when stretched. NPR materials have been demonstrated to exhibit enhanced shear resistance, indentation resistance (Alderson et al., 1994, 2000) and fracture toughness (Choi and Lakes, 1996). Moreover, NPR materials have been shown to possess extraordinary damping properties (Chen and Lakes, 1996), acoustic properties (Chekkal et al., 2010) and dynamic crushing performance (Scarpa et al., 2002). Hence, NPR materials find potential applications in many fields (Lakes, 1993; Liu, 2006).

Besides natural NPR materials found in some rocks and minerals, a wide variety of auxetic materials have been created and fabricated using different deformation mechanisms (Lakes, 1991), including polymeric and metallic foams (Lakes, 1987), microporous polymers (Evans, 1991; Alderson and Evans, 1992), carbon fiber laminates (Evans et al., 2004) and honeycomb structures (Prall and Lakes, 1997; Lakes and Witt, 2002). Under finite deformation, material properties are generally dependent on the deformation and show severe nonlinear behavior (Prall and Lakes, 1997; Smith et al., 1999; Scarpa and Smith, 2004). Therefore, the optimized properties, such as NPR, based on small deformation theory may degrade or even reverse under finite deformation. Recently, periodic nonlinear affine unimode metamaterials have been constructed from

\* Corresponding author. Tel.: +45 4525 4266.

E-mail address: [fwan@mek.dtu.dk](mailto:fwan@mek.dtu.dk) (F. Wang).

rigid bars and pivots to achieve fixed Poisson's ratio over a large strain range (Milton, 2013). In this study, we will investigate material design under finite deformation using topology optimization.

Over the last two decades, topology optimization methods have been demonstrated to be an attractive design approach in many fields covering mechanical and structural engineering, fluid dynamics, optical engineering, and more (Bendsøe and Kikuchi, 1988; Bendsøe and Sigmund, 2003). Topology optimization has also shown its applicability to create novel materials with enhanced properties. In this way, material properties are tailored through a redistribution of the material layout in the microstructure. Examples include NPR materials (Sigmund, 1994, 1995; Larsen et al., 1997; Schwerdtfeger et al., 2012; Andreassen et al., 2014), materials with negative thermal expansion coefficient (Sigmund and Torquato, 1997), novel piezoelectric properties (Silva et al., 1998; Sigmund et al., 1998), enhanced dissipation (Yi et al., 2000; Andreassen et al., 2014), photonic and phononic bandgap materials (Cox and Dobson, 1999; Sigmund and Jensen, 2003) and metamaterials with negative permeability (Diaz and Sigmund, 2010). Moreover, in order to ensure manufacturability and control of minimum feature sizes of the topology optimized designs, different techniques have been developed (Haber et al., 1996; Bourdin, 2001; Bruns and Tortorelli, 2001; Sigmund, 2007, 2009; Wang et al., 2011).

So far most examples of topological material design have been performed using linear finite element analysis valid for small displacements and linear elasticity. In this case the effective material properties can be computed by a standard homogenization approach for unit cells of periodic microstructures, see e.g. the review in Hassani and Hinton (1998a–c). A homogenization theory for the effective properties of nonlinear composite materials has been presented by Talbot and Willis (1985) and Ponte Castañeda (1991). However, determining the homogenized properties of nonlinear materials at finite deformation is still an active research area. Important contributions in this field have been made by Hill (1972), Ponte Castañeda and Zaidman (1996), Miehe (2003), Yvonnet and He (2010), Lamari et al. (2010), and Clement et al. (2012). Due to the complexity of the homogenization procedure under finite deformation, topology optimization methods have only recently been extended to tailor materials for prescribed nonlinear properties. In Nakshatrala et al. (2013) the effective material properties are evaluated under finite deformation using a numerical homogenization procedure and incorporated into multiscale topology optimization that allows for locally varying microstructures.

The present study is closely related to the work of Nakshatrala et al. (2013). However, we will focus on design of materials with prescribed stress–strain curves and Poisson's ratio under finite deformation. We restrict ourselves to material design based on numerical tensile experiments where the material is uniformly stretched, which allows us to circumvent the computationally intensive nonlinear homogenization. The geometrically nonlinear behavior of the periodic microstructure is simulated using a total Lagrangian finite element formulation, and solved by a Newton–Raphson algorithm. Two optimization problems of prescribed stress–strain curves and Poisson's ratio are formulated to minimize the errors between actual and prescribed properties for a target axial strain range. Two dimensional truss-based and continuum materials are designed using the proposed optimization formulation.

As an additional challenge, previous studies on structural topology optimization under finite deformation for stiffness optimization and design of compliant mechanisms (Buhl et al., 2000; Pedersen et al., 2001; Bruns and Tortorelli, 2003; Yoon and Kim, 2005; Klarbring and Stromberg, 2013), have shown that excessive deformation observed in low density elements may lead to numerical instability of the Newton–Raphson solution procedure. Different computational approaches have been introduced to circumvent the numerical instability (Buhl et al., 2000; Bruns and Tortorelli, 2003; Yoon and Kim, 2005). More recently, hyperelastic material models have been employed in structural topology optimization (Klarbring and Stromberg, 2013) to remedy the problem. This approach works well for problems that are dominated by tensile forces and we have adapted this approach for our continuum examples where this is the case. For problems involving significant compression of void regions we have recently proposed a new interpolation scheme based on a linear modeling of the void regions (Wang et al., 2014).

The paper is organized as follows. In Section 2, we introduce the physical model to characterize the material properties in a tensile test under finite deformation and state the corresponding finite element formulation. In Section 3, we formulate the optimization problems for designing materials with prescribed stress–strain curves and with prescribed Poisson's ratio for both truss-based and continuum materials. Section 4 is dedicated to presenting optimized material layouts for prescribed nonlinear properties as well as the corresponding performances. The paper ends with the conclusions in Section 5.

## 2. Characterization of material behavior in a tensile test

In a periodic material, effective material properties can be characterized using a unit cell as illustrated in Fig. 1(a). Homogenization methods can be used to calculate the effective material properties in the small deformation regime. However, when the material undergoes finite deformation, the material properties will be strongly dependent on the deformation and the effective material properties have to be calculated for each deformation state (Yvonnet et al., 2009). In order to simplify the problem, this paper focuses on tensile deformation tests.

In a tensile test, materials are uniformly stretched either longitudinally or transversely. The material behavior can be characterized using the unit cell subjected to boundary displacements as shown in Fig. 1(b) and stated in Eq. (1). The unit cell is fixed at the lower left corner. For each node pair on the left and right boundaries, periodic boundary conditions are employed in the transverse displacements, given as  $v_1 = v_{01}$ , and a constant displacement difference,  $u$ , is assumed longitudinally as  $u_1 - u_{01} = u$ . For each node pair on the lower and upper boundaries, periodic boundary conditions are

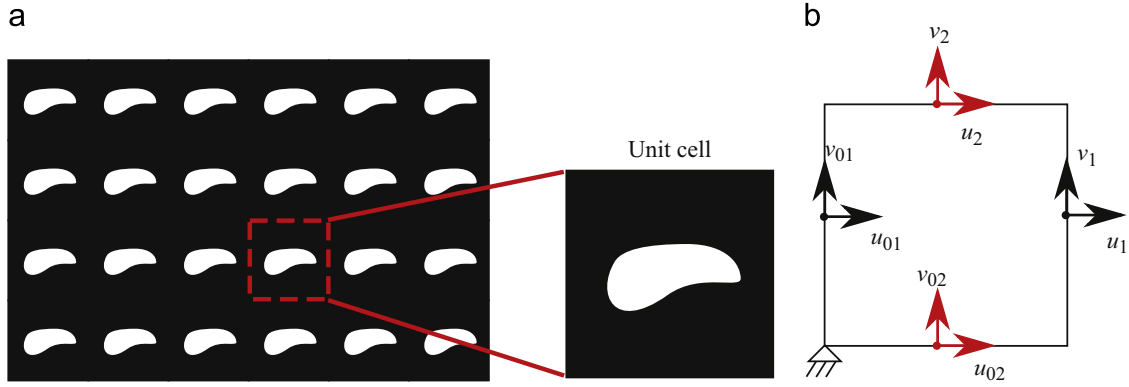


**Fig. 1.** (a) Schematic illustration of a unit cell, i.e. the periodic microstructure. (b) Illustration of the applied boundary displacements for the unit cell problem.

employed in the longitudinal displacements as  $u_2 = u_{02}$ , and a constant displacement difference,  $v$ , is assumed transversely as  $v_2 - v_{02} = v$ :

$$u_1 - u_{01} = u, \quad v_1 = v_{01}; \quad u_2 = u_{02}, \quad v_2 - v_{02} = v. \quad (1)$$

Using the proposed model, the longitudinal and transverse tensile tests are mimicked by prescribing the longitudinal and transverse displacement differences, respectively, i.e. a prescribed longitudinal displacement difference  $u = u_0$  mimics a longitudinal tensile test. The corresponding averaged axial engineering stress can be calculated as

$$\bar{\sigma} = \frac{F}{A} \quad (2)$$

with  $F$  as the axial force in the tensile test and  $A$  as the cross-sectional area in the reference configuration. In the present model, the axial force  $F$  is equal to the internal force on the right boundary. The same approach can be applied to characterize the axial engineering stress in a transverse tensile test by specifying the transverse displacement difference as  $v = v_0$ .

In this study, we define Poisson's ratio of materials under finite deformation as the negative ratio between transverse to axial strain in a longitudinal tensile test, or as the negative ratio between longitudinal to axial strain in a transverse tensile test. Assuming a unit cell of unit dimension, Poisson's ratios in both the directions are calculated by

$$\nu_{12} = -\frac{v}{u_0}, \quad \nu_{21} = -\frac{u}{v_0}, \quad (3)$$

i.e. we obtain a secant Poisson's ratio as opposed to a tangential formulation which would imply, e.g.  $\nu_t = \Delta v / \Delta u_0$ .<sup>1</sup>

Using a finite element discretization, the static equilibrium of the unit cell under finite deformation is governed by the following equation:

$$\mathbf{r} = \mathbf{f}^{\text{ext}} - \mathbf{f}^{\text{int}}(\mathbf{u}) = 0 \quad (4)$$

where  $\mathbf{r}$  is the residual nodal force vector,  $\mathbf{f}^{\text{ext}}$  is the external nodal force vector,  $\mathbf{f}^{\text{int}}(\mathbf{u})$  is the internal nodal force vector that is dependent on the nodal displacement vector,  $\mathbf{u}$ . The internal nodal force vector is defined by

$$\mathbf{f}^{\text{int}}(\mathbf{u}) = \frac{\partial (\int_v W(\mathbf{u}) dv)}{\partial \mathbf{u}} \quad (5)$$

where  $W(\mathbf{u})$  is the stored elastic energy. The detailed calculation of  $\mathbf{f}^{\text{int}}(\mathbf{u})$  can be found e.g. in Zienkiewicz and Taylor (2005).

The static equilibrium, Eq. (4), is solved iteratively using the Newton–Raphson method, with the incremental equation given as

$$\mathbf{K}_t \Delta \mathbf{u} = \mathbf{r} \quad (6)$$

where the nodal displacement vector is updated by  $\mathbf{u} = \mathbf{u} + \alpha \Delta \mathbf{u}$  with  $\alpha = 0.5$  to stabilize the Newton–Raphson iterations and  $\mathbf{K}_t = -\partial \mathbf{r} / \partial \mathbf{u}$  is the tangent stiffness matrix. The formulation of the tangent stiffness matrix is described in standard books on non-linear finite element theory (Zienkiewicz and Taylor, 2005) and is not presented here.

In order to validate the proposed model, we compare results based on Eqs. (1)–(6) with the results extracted from a macroscale numerical tensile test of a finite structure. The model for the longitudinal tensile test is shown in Fig. 2(a), where the periodic boundary conditions on the transverse displacements are implemented on the left and right boundaries to ensure uniform stretching.

<sup>1</sup> In this paper, we aim at providing deformation independent Poisson's ratio, meaning that the two formulations would be equal.

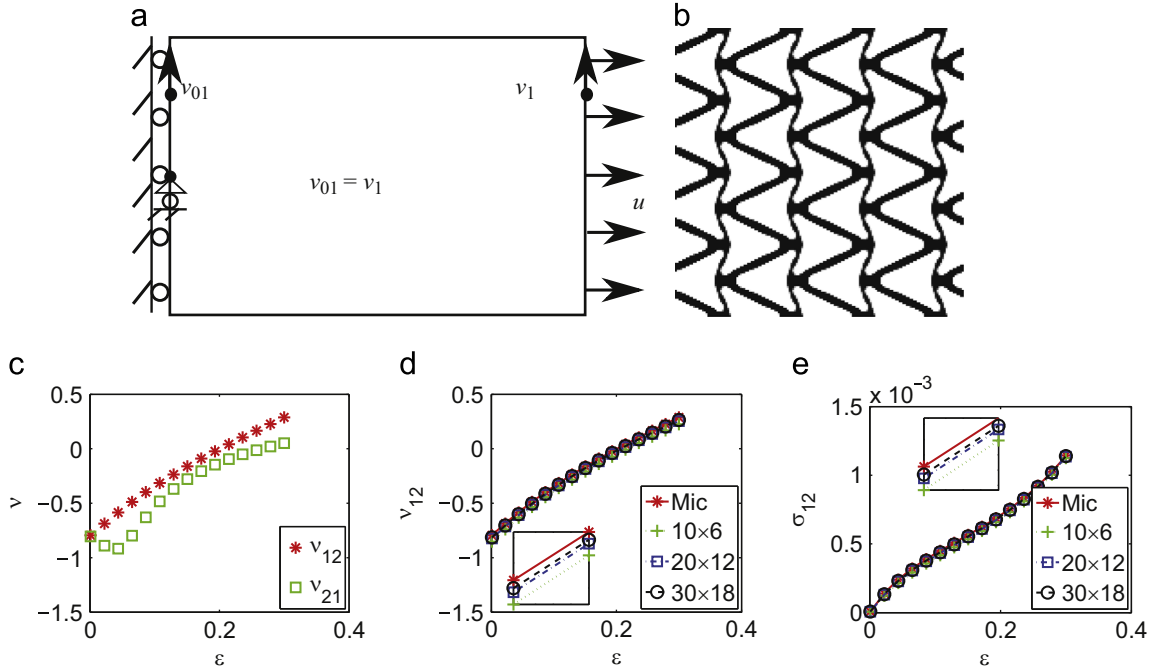


**Fig. 2.** Evaluation of the proposed microstructural model. (a) Schematic illustration of the numerical simulation model for a macroscale tensile test. (b) Topology optimized material with NPR. (c) Poisson's ratios versus strain under finite deformation. (d) Comparison of Poisson's ratio from micro- and macro-evaluations. (e) Comparison of the axial engineering stress from micro- and macro-evaluations.

A topology optimized NPR material presented by [Larsen et al. \(1997\)](#) (see [Fig. 2\(b\)](#)) is analyzed. This material shows isotropic material properties with effective Young's modulus of  $E = 0.0072E_0$  and Poisson's ratio of  $\nu = -0.80$  for small deformations. The base material (black) has stiffness  $E_0$  and Poisson's ratio  $\nu = 0.3$ . [Fig. 2\(c\)](#) shows the effective Poisson's ratios in both directions versus strain when considering finite deformations. It is seen that this optimized NPR material exhibits strongly nonlinear Poisson's ratio behavior and additionally non-isotropic performance under finite deformation. Three different macrostructures, consisting of  $10 \times 6$ ,  $20 \times 12$  and  $30 \times 18$  unit cells are simulated. The comparison between  $\nu_{12}$  and  $\sigma_{12}$  from micro- and macro-evaluations is presented in [Fig. 2\(d\)](#) and (e), respectively. There are no significant differences between micro- and macro-evaluations for both the Poisson's ratio and the axial engineering stress. The enlarged subplots demonstrate that the values from the macrostructure model converge to the results from the proposed microstructural model, as the number of unit cells in the macrostructure increases. Hence we conclude that the proposed model adequately characterizes the material properties in a tensile test under finite deformation.

### 3. Optimization problems

This study focuses on designing materials for two different effective properties under finite deformation. In the first case, nonlinear materials with prescribed stress–strain curves are considered. In the second case, nonlinear materials with prescribed Poisson's ratio are designed. The optimization formulations for these two optimization problems are described in detail in this section.

#### 3.1. Design parameterizations

One approach for modeling and optimizing microstructures is to use truss-based structures ([Sigmund, 1994](#)). In order to perform computational optimization, a variable,  $x_e$ , is assigned to a truss element,  $e$ , and the design variable is employed to represent the cross-sectional area of the truss element.

Alternatively, microstructures can be modeled as 2D continuum structures. In this case, the element design variable,  $x_e$ , is introduced to represent material occupation in element  $e$ . The element property is here interpolated using the solid isotropic material with penalization (SIMP) model ([Bendsøe and Sigmund, 1999](#)) stated as

$$E_e = \bar{x}_e^p (E_1 - E_0) + E_0 \quad (7)$$

where  $E_1$  is Young's modulus of the base material (black),  $E_0 = 10^{-9}$  is employed to represent void regions (white), and  $p=3$  is a standard penalization factor. In order to enhance the discreteness of the final designs, a hyperbolic tangent threshold projection is employed to generate physical design variables  $\bar{x}_e$  ([Wang et al., 2011](#)). The element,  $e$ , is occupied by solid material when  $\bar{x}_e = 1$  and by void when  $\bar{x}_e = 0$ .

The physical design variable,  $\bar{x}_e$ , is calculated by

$$\bar{x}_e = \frac{\tanh(\beta\eta) + \tanh(\beta(\tilde{x}_e - \eta))}{\tanh(\beta\eta) + \tanh(\beta(1 - \eta))} \quad (8)$$

with  $\tilde{x}_e$  as the filtered design variable calculated by

$$\tilde{x}_e = \frac{\sum_{j \in N_e} w(\mathbf{y}_j) v_j x_j}{\sum_{j \in N_e} w(\mathbf{y}_j) v_j} \quad (9)$$

where  $\mathbf{y}_j$  is the position of the center of element  $j$ ,  $v_j$  is the corresponding volume,  $N_e$  is the neighborhood of element  $e$  within a certain filter radius  $r$  specified by  $N_e = \{j \mid \|\mathbf{y}_j - \mathbf{y}_e\| \leq r\}$ , and  $w(\mathbf{y}_j)$  is the weighting factor defined as  $w(\mathbf{y}_j) = r - \|\mathbf{y}_j - \mathbf{y}_e\|$ . In this paper, the filter radius is set to be  $r = a/8$  with  $a$  as the size of the unit cell.

This approach has been suggested in Sigmund (2007) and Xu et al. (2010) and has been shown to yield discrete designs. As an additional benefit, based on the threshold projection, different design realizations in the manufacturing process can be approximated by choosing different thresholds  $\eta$ . This has been demonstrated to enhance design robustness (Wang et al., 2011).

In most studies of topology optimization of nonlinear structures, the St. Venant–Kirchhoff model is employed to describe the material behavior under finite deformation. However, it is well-known that the St. Venant–Kirchhoff model fails when the materials undergo excessive compression. In this paper, we employ a modified St. Venant–Kirchhoff model to describe the material behavior following the study of Klarbring and Stromberg (2013), given as

$$W = \frac{1}{2} \lambda (J - 1)^2 + \frac{\mu}{4} (I_C - 2I_C + 3), \quad (10)$$

here  $\lambda$  and  $\mu$  are the Lamé material parameters,  $J = \det(\mathbf{F})$  with  $\mathbf{F}$  as the deformation gradient,  $I_C = \text{tr}(\mathbf{C})$  with  $\mathbf{C} = \mathbf{F}^T \mathbf{F}$  as right Cauchy strain, and  $I_C = \text{tr}(\mathbf{C}^2)$ . The relations between Young's modulus  $E$ , Poisson's ratio  $\nu$  and the Lamé parameters for the considered plane strain assumption are  $\lambda = E\nu/((1-\nu)(1-2\nu))$  and  $\mu = E/(2(1+\nu))$ . As shown in Klarbring and Stromberg (2013), this model delays the onset of the numerical instability problems encountered with low density elements.

### 3.2. Optimization formulations

The optimization problem for designing a material with prescribed nonlinear properties can be formulated as to minimize the errors between actual and prescribed properties for a given strain range, stated as

$$\begin{aligned} \min_{\mathbf{x}} \max_{\varepsilon_i} f &= (c(\varepsilon_i) - c^*(\varepsilon_i))^2, \quad i = 1, \dots, n \\ \text{s.t. } \mathbf{r} &= \mathbf{0} \\ \mathbf{v}^T \mathbf{x} &\leq v^* \\ \mathbf{x}_{\min} &\leq \mathbf{x} \leq \mathbf{x}_{\max} \end{aligned} \quad (11)$$

where  $\varepsilon_i \in [\varepsilon^0, \varepsilon^1]$  is the target strain range,  $c(\varepsilon_i)$  and  $c^*(\varepsilon_i)$  are the actual and prescribed properties for a given target strain  $\varepsilon_i$ ,  $n$  is the total number of target strains,  $\mathbf{v}$  is the elemental volume vector,  $v^*$  is a prescribed maximum material volume and  $\mathbf{x}_{\min}$  and  $\mathbf{x}_{\max}$  are the minimum and maximum values of the design variables,  $\mathbf{x}$ .

The property,  $c^*$ , is set to be the axial engineering stress when designing materials with prescribed stress–strain curves, given as  $c(\varepsilon_i) = \bar{\sigma}(\varepsilon_i)$  and  $c^*(\varepsilon_i) = \sigma^*(\varepsilon_i)$ . Based on the finite element analysis, the averaged axial engineering stress, given by Eq. (2), can be calculated by

$$\bar{\sigma} = \mathbf{l}^T \mathbf{f}^{\text{int}}(\mathbf{u})/A \quad (12)$$

where  $\mathbf{l}$  is a zero vector with unit entries at the longitudinal degrees of freedom on the right boundary in the longitudinal tensile test or with the ones at the transverse degrees of freedom on the upper boundary in the transverse tensile test.

When designing materials with prescribed Poisson's ratio, the property,  $c^*$ , is set to be Poisson's ratio as  $c(\varepsilon_i) = \nu(\varepsilon_i)$  and  $c^*(\varepsilon_i) = \nu^*(\varepsilon_i)$ . In order to ensure non-vanishing stiffness of the materials along the axial directions, constraints on the average axial engineering stresses are additionally implemented in this case, stated as  $\bar{\sigma}(\varepsilon_i) \geq \sigma^*$ .

Based on the chosen parameterization, the adjoint method is employed to compute the sensitivity of the objective and constraints, collectively denoted  $f$ , with respect to a design variable  $x_e$ , given as

$$\frac{\partial f}{\partial x_e} = \frac{\partial f(\mathbf{u}, \mathbf{x})}{\partial x_e} + \lambda^T \frac{\partial \mathbf{r}}{\partial x_e} \quad (13)$$

with  $\lambda$  being an adjoint variable vector, which is solved by

$$(\mathbf{K}_t)^T \lambda = \left( \frac{\partial f(\mathbf{u}, \mathbf{x})}{\partial \mathbf{u}} \right)^T \quad (14)$$

where  $\mathbf{K}_t$  is the tangent stiffness at the converged solution and the superscript,  $T$ , indicates the transpose of a matrix. See additional details in Pedersen et al. (2001).

Based on the sensitivity analysis, the microstructure is iteratively updated using the Method of Moving Asymptotes (MMA) from Svanberg (1987). The numerical implementation of the optimization problem follows the standard procedure outlined in many references and is not presented here.

In order to ensure 2D black-white continuum designs, a continuation scheme is employed to increase  $\beta$  in Eq. (8). In this paper,  $\beta$  is updated every 20 iterations using  $\beta = 2 \times \beta$ , with a maximal value of  $\beta_{\max} = 50$ .

#### 4. Results

In this section, we utilize the aforementioned optimization formulation to design materials with different nonlinear properties. The first part focuses on designing truss-based materials. Both materials with prescribed stress–strain curves and materials with prescribed Poisson's ratios are designed using Eq. (11). In the second part, 2D continuum materials are designed for prescribed Poisson's ratios with a plane strain assumption.

In the truss-based material design, the box constraints for the design variables are  $10^{-8} \leq x_e \leq 100$ , the total volume of material is set to be 200, and Young's modulus is  $E = 1$ . The truss-based microstructures are constructed from a  $4 \times 4$  node full ground structure with 120 potential bars, i.e. all nodes may be connected with bars allowed to overlap. In order to illustrate all nodal connections in the optimized microstructural configurations, the optimized microstructure is presented in both a regular pattern and a perturbed nodal connectivity pattern. The symmetry of microstructures is enforced along the diagonal and axial directions in all the truss-based designs. This ensures that optimized materials perform identically in both the longitudinal and transverse tensile tests, hence, only the longitudinal tensile test is considered. To ease the illustration of the optimized configurations, only truss elements with cross-sectional area bigger than or equal to 0.02 are shown, with the thickness of bars indicating the corresponding area.

In 2D continuum material design, the microstructures are discretized by  $80 \times 80$  bilinear square elements. The base material parameters are set as  $E_1 = 1$  and  $\nu = 0.3$  and the prescribed material volume fraction is 0.4. Different from the truss-based material design, the design symmetry is not enforced along the diagonal direction in this case. Hence both longitudinal and transverse tensile tests are simulated in the optimization procedure, in order to ensure the performance of optimized materials in both tests.

##### 4.1. Truss-based materials with prescribed stress–strain curves

In the first example, we validate the optimization formulation by designing a pseudo-material with the same stress–strain curve as the cross shown in Fig. 3(a). As seen in the right panel in Fig. 3(a), this material displays nearly zero stiffness when the axial strain is below a critical strain of  $\varepsilon = \sqrt{2} - 1$ , corresponding to the stretch ratio where originally diagonal bars become horizontal, and shows a constant stiffness beyond the critical strain.

Fig. 3(b) presents the optimized design and the corresponding performance. The performance of the material, represented by the line, demonstrates that the optimized material can achieve almost target performance as represented by the asterisks. However, the optimized design exhibits a more complicated configuration compared to the target structure. To simplify microstructural configurations, the method presented by Sigmund (1995) is employed to penalize short or long bars. The corresponding objective is modified to minimize the weight of the microstructures subjected to a tolerated performance, as

$$\begin{aligned} \min_{\mathbf{x}} \max_{\varepsilon_i} \quad & W = \sum v_e x_e \\ \text{s.t.} \quad & \mathbf{r} = 0 \\ & (\bar{\sigma}(\varepsilon_i) - \sigma^*(\varepsilon_i))^2 < \delta^2, \quad i = 1, \dots, n \\ & \mathbf{x}_{\min} \leq \mathbf{x} \leq \mathbf{x}_{\max} \end{aligned} \quad (15)$$

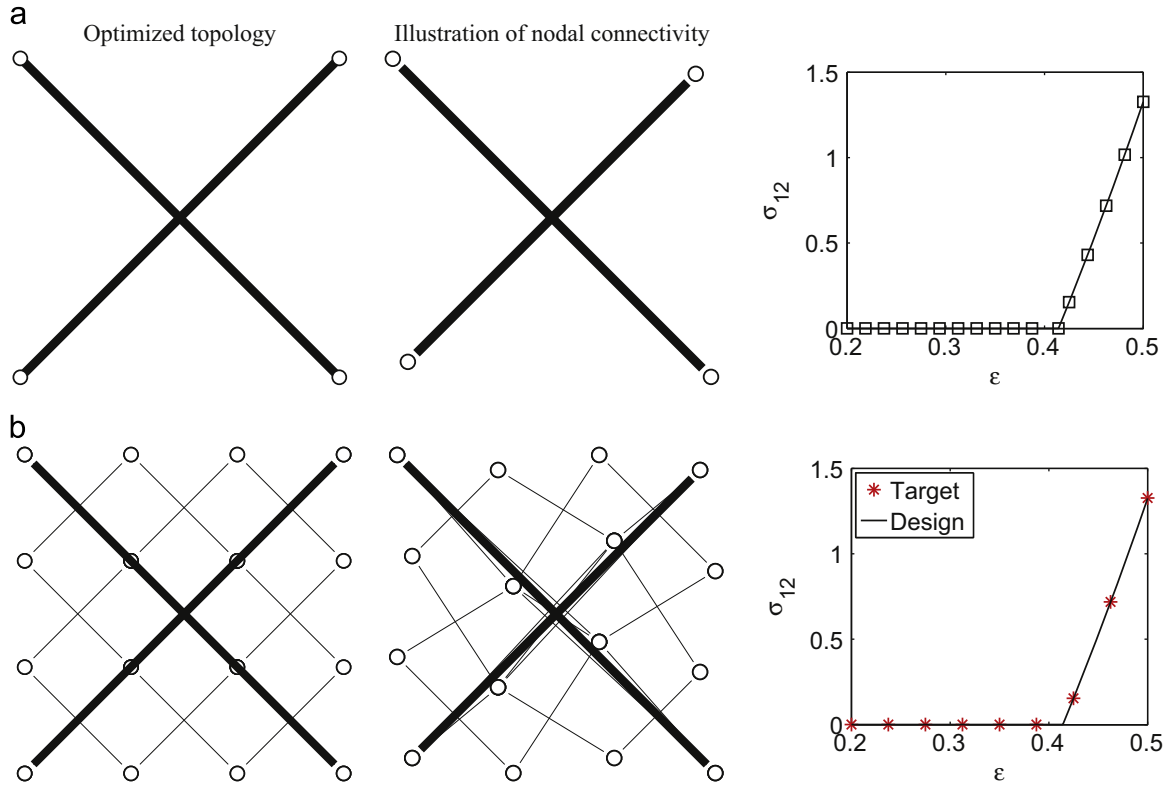
Here,  $v_e$  is the modified length of a bar element defined by  $v_e = l_e(l_t/l_e)^\alpha$ . It is introduced to penalize solutions with short or long bars,  $l_e$  is the length of the bar element,  $l_t$  is the preferred length, and bars longer or shorter than  $l_t$  will be penalized with  $\alpha$  being positive or negative, respectively.  $\delta$  is the allowed tolerance of the target performance.

Fig. 4(a) and (b) shows the final designs with penalization on short and long bars, respectively. It is seen that the optimized microstructural configurations are significantly simplified by penalizing short or long bars, while keeping equally good performance.

In the second example, we aim at designing materials having a rubber-like response in a target strain range of  $\varepsilon_i \in [0.2, 0.5]$ . The design strain range is subdivided into three intervals, and the target stresses are set to have different slopes in these three intervals as shown by the asterisks in Fig. 5. The slopes of the stress–strain curves in the three intervals are 3.0, 0.2 and 20. Fig. 5 shows two different optimized microstructural configurations obtained with penalizations on short or long bars, respectively, as well as the corresponding performances. Both optimized designs achieve a good agreement with the target, with the corresponding tolerance set to be  $\delta = 0.05$ .

In the third example, we modify the strain range to  $\varepsilon_i \in [0.0, 0.3]$  but keep the slopes of the target stress–strain curve identical to the ones in Fig. 5 with the same tolerance of  $\delta = 0.05$ . Thus, we specify the required response also for vanishing strain, i.e. the linear response of the truss material. Fig. 6 shows the two optimized configurations with penalization on short





**Fig. 3.** (a) Performance of a pseudo material consisting of crosses. Left: Microstructural configuration of the pseudo-material. Middle: Microstructural configuration with a perturbed nodal connectivity pattern. Right: Stress-strain curve in the strain range of  $\varepsilon_i \in [0.2, 0.5]$  under finite deformation. (b) Optimized material and corresponding performance. The thickness of the bars indicates the cross-sectional area in all truss-based results.

or long bars, respectively, and their corresponding performance. It is seen that the target response is met at the expense of quite complicated microstructures both when favoring long and short bars.

#### 4.2. Truss-based materials with prescribed Poisson's ratio

In this subsection, we employ the proposed optimization formulation in Eq. (11) to design materials for different prescribed Poisson's ratios in the target axial strain range  $\varepsilon_i \in [0.0, 0.3]$ . Moreover, materials are also designed to achieve the prescribed Poisson's ratios under small deformation, in order to compare the corresponding performances. All the optimized designs presented in this section are obtained by penalizing bars with length longer than 0.4 using  $l_t = 0.4$  and  $\alpha = -3$ .

In the first example, we aim at designing materials for a target Poisson's ratio of  $\nu^* = 1.0$ . Fig. 7(a) shows the microstructure optimized for small deformation and the corresponding performance under finite deformation. The optimized material achieves a Poisson's ratio of  $\nu = 0.980$  for vanishing strain. However, for larger strain the Poisson's ratio increases, as seen in the right panel in Fig. 7(a). Fig. 7(b) shows the optimized microstructure considering finite deformation. It is seen in the performance plot (the right panel in Fig. 7(b)) that the optimized material exhibits a nearly constant Poisson's ratio with an average value of  $\bar{\nu} = 0.998$  and a small variation within  $\pm 3.3\%$ .

Fig. 8 depicts the optimized microstructures for the target Poisson's ratio of  $\nu^* = 0.5$ . The optimized microstructure obtained under small deformation, see Fig. 8(a), exhibits increased Poisson's ratio for larger strain values. On the contrary, the optimized microstructure obtained under finite deformation, see Fig. 8(b), shows nearly constant Poisson's ratio with an average value of  $\bar{\nu} = 0.500$ . The variation in the target axial strain is within  $\pm 1.5\%$ .

For illustrative purposes we have in Fig. 9 included an optimized material for the target Poisson's ratio of  $\nu^* = 0.0$ , obtained under small deformation. Due to the decoupling between longitudinal and transverse deformations with the optimized configuration, the optimized material exhibits a constant Poisson's ratio at arbitrary strain levels.

As the final examples, Figs. 10 and 11 show optimized NPR microstructures for  $\nu^* = -0.5$  and  $\nu^* = -1.0$ . As opposed to the optimized materials for small deformations in Figs. 10(a) and 11(a), the finite deformation formulation (see Figs. 10(b) and 11(b)) produces a nearly constant Poisson's ratio. However, for  $\nu^* = -1.0$  a somewhat larger variation is noted, especially when the axial strain approaches 0.3, indicating the limitations of the chosen ground structure for obtaining the prescribed properties.

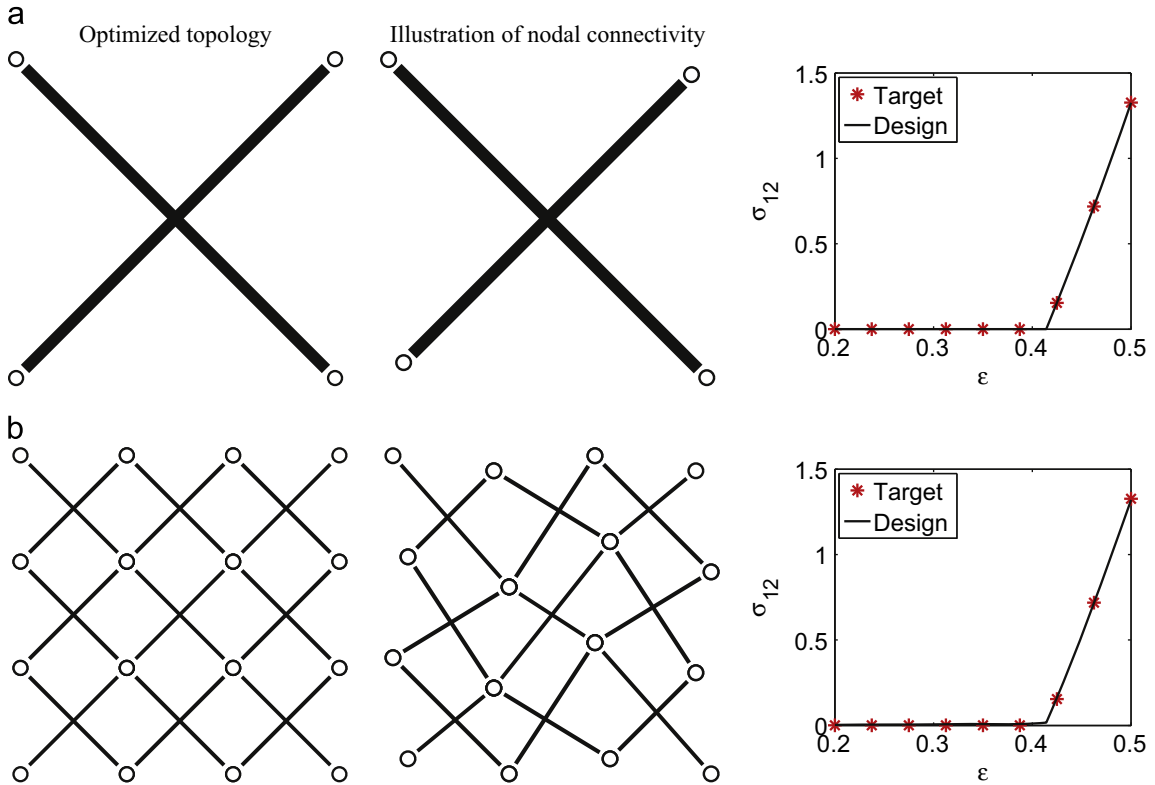


**Fig. 4.** (a) Optimized microstructure with penalization on short bars to achieve the performance of a cross. (b) Optimized microstructure with penalization on long bars to achieve the performance of a cross.

An interesting hypothesis is that a vanishing slope of the Poisson's ratio curve at small strain levels may ensure a flat curve also for finite strain levels. This would enable us to optimize the behavior using small displacements with an additional constraint on the curve slope, instead of simulating the behavior for large displacements which is significantly more costly. It is seen that Poisson's ratio curve in Fig. 11(a) is very flat for small strains, however, the performance still degrades for large strains. Moreover, a kink at small strain levels is observed in the curve in Fig. 8(b) although the curve is very flat for larger strains. Thus, the small strain properties are not directly linked to the finite strain performance and therefore a corresponding optimization formulation cannot readily be used to guarantee the performance for large strains.

#### 4.3. 2D continuum materials with prescribed Poisson's ratio

In the following, we aim at designing 2D continuum materials for different prescribed Poisson's ratios. The target axial strain range is as for the truss-based materials, given as  $\epsilon_i \in [0.0, 0.3]$ . We here present optimized microstructures generated using a fixed threshold of  $\eta = 0.5$  in Eq. (8).

In the first case, we use a target of  $\nu^* = -1.0$ . As for truss-based material designs, we design 2D continuum materials for both small and finite deformations to compare the corresponding performance.

Fig. 12(a) shows the optimized material under small deformation. The left panel shows the optimized microstructure and the middle panel displays the optimized material consisting of  $4 \times 4$  periods of the microstructures. The optimized material possesses Poisson's ratios of  $\nu_{12} = -0.908$  and  $\nu_{21} = -0.907$  under small deformation. However, Poisson's ratios are strongly dependent on the axial strain as seen in the right panel in Fig. 12(a). Fig. 12(b) shows the optimized material under finite deformation. The optimized material here exhibits average Poisson's ratios of  $\bar{\nu}_{12} = -0.838$  and  $\bar{\nu}_{21} = -0.838$ . The variation in the target axial strain range is within  $\pm 1.6\%$ . Thus, the constant value of  $\nu$  is obtained at the expense of a value somewhat higher than  $-1.0$ .

In the second example, we design materials with enhanced symmetry along both axial directions. The optimized material for small deformation is shown in Fig. 13(a) and the corresponding Poisson's ratios under small deformation are  $\nu_{12} = -0.929$  and  $\nu_{21} = -0.931$ . Compared with the previous design under small deformation, this symmetrical material shows a slightly better performance in terms of meeting the prescribed target. This is somewhat unexpected but indicates that the structure in Fig. 12(a) is a local minimum. Fig. 13(b) shows the optimized material for finite deformation. As in the previous case, the material exhibits nearly constant Poisson's ratio under finite deformation. The average Poisson's ratios in



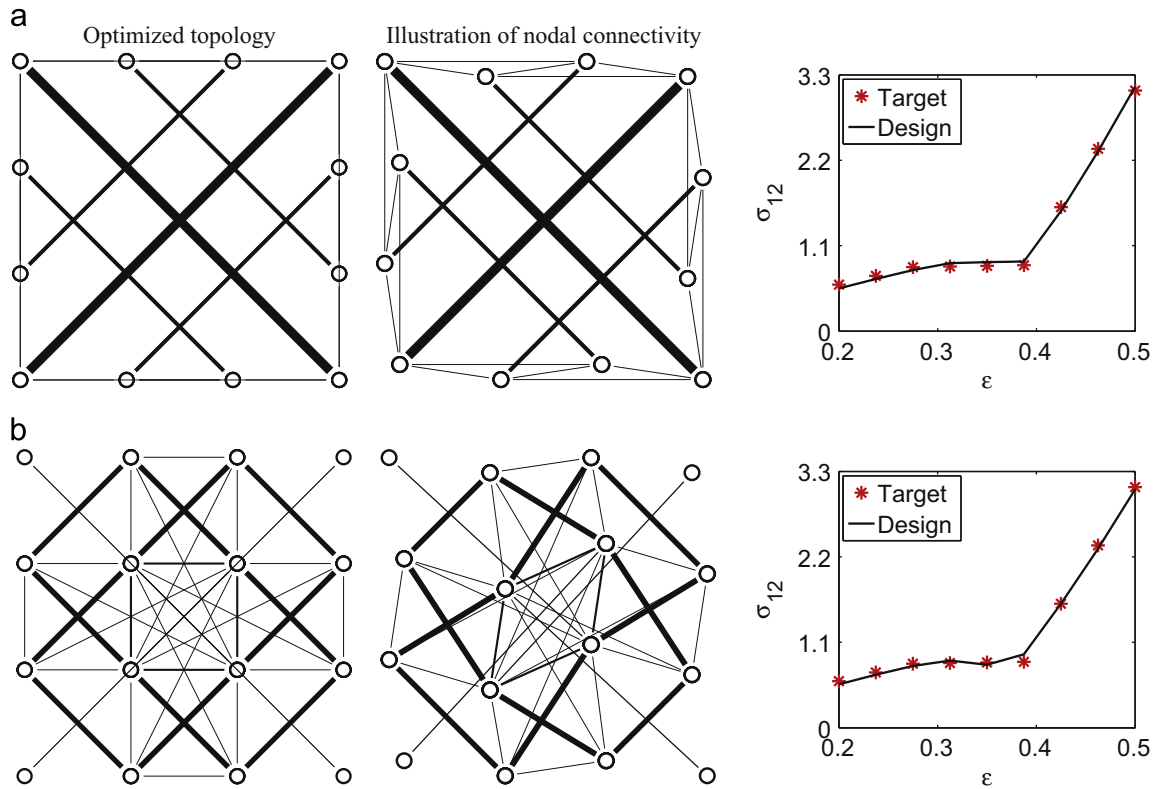


**Fig. 5.** Optimized microstructures for rubber-like responses in a target strain range of  $\epsilon_i \in [0.2, 0.5]$ . (a) Optimized material with penalization on short bars. (b) Optimized material with penalization on long bars.

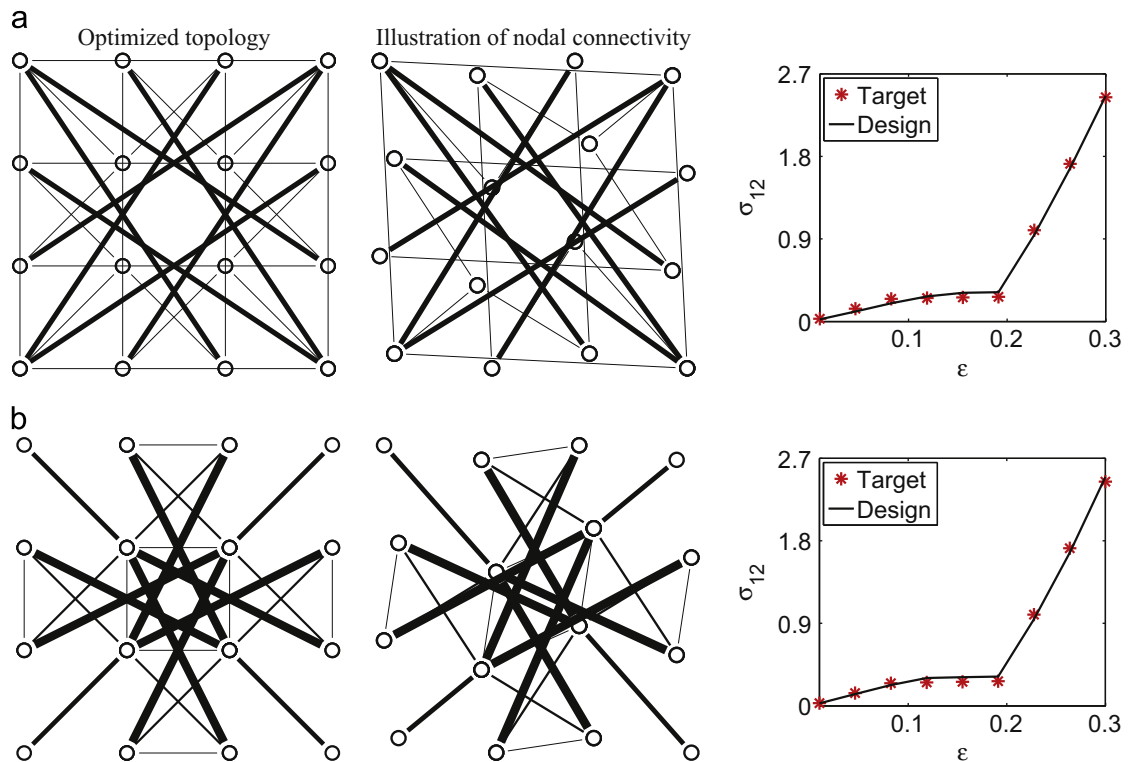


**Fig. 6.** Optimized microstructures for rubber-like responses in a target strain range of  $\epsilon_i \in [0.0, 0.3]$ . (a) Optimized microstructure with penalization on short bars. (b) Optimized microstructure with penalization on long bars.

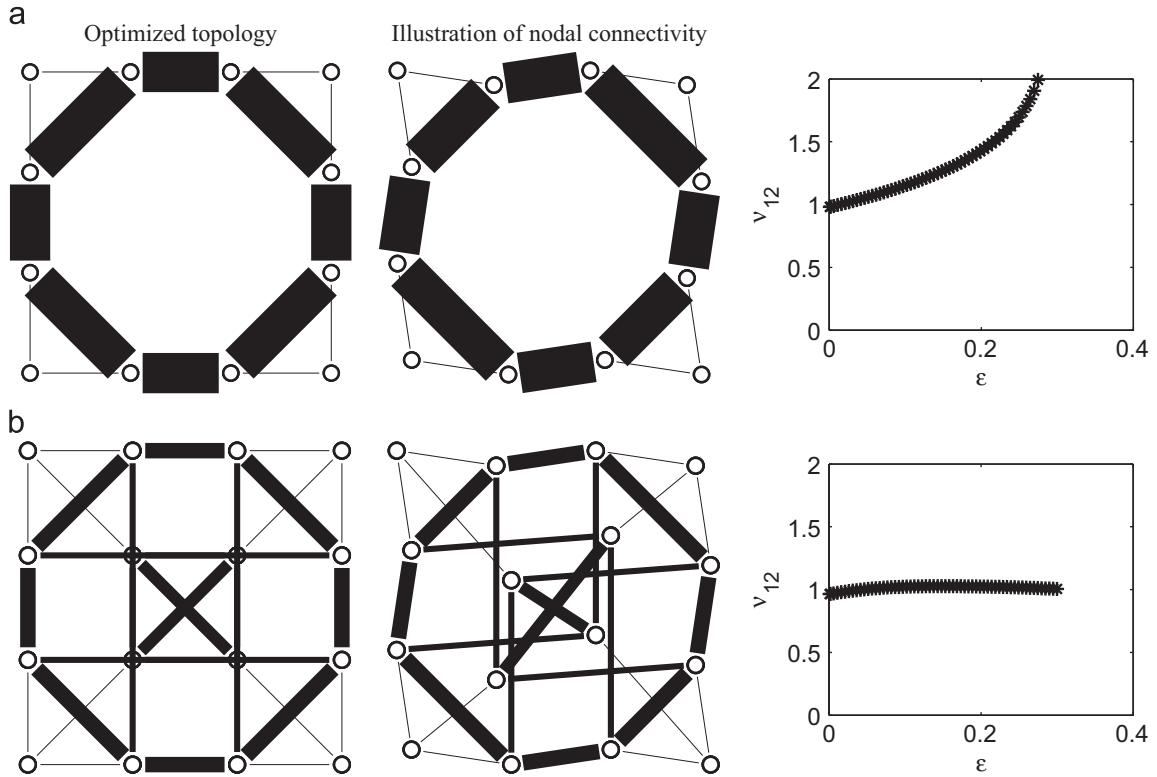


**Fig. 7.** Optimized materials for  $\nu^* = 1.0$  and corresponding performances under finite deformation. (a) Optimized material under small deformation and corresponding Poisson's ratio under finite deformation. (b) Optimized material under finite deformation and corresponding Poisson's ratio under finite deformation.

both directions are  $\bar{\nu}_{12} = -0.839$  and  $\bar{\nu}_{21} = -0.839$  with a variation within  $\pm 5.7\%$ . The biggest variations are observed at an axial strain of  $\varepsilon_i = 0.3$ .

In the following case, we design materials for prescribed Poisson's ratio of  $\nu^* = -0.5$ . The asymmetrical and symmetrical optimized materials are presented in Fig. 14(a) and (b), respectively. The asymmetrical optimized material achieves average Poisson's ratios of  $\bar{\nu}_{12} = -0.501$  and  $\bar{\nu}_{21} = -0.501$  and a variation within  $\pm 2.0\%$ . With the symmetrical optimized material we obtain  $\bar{\nu}_{12} = -0.510$  and  $\bar{\nu}_{21} = -0.510$ , with a variation of  $\pm 7.4\%$ .

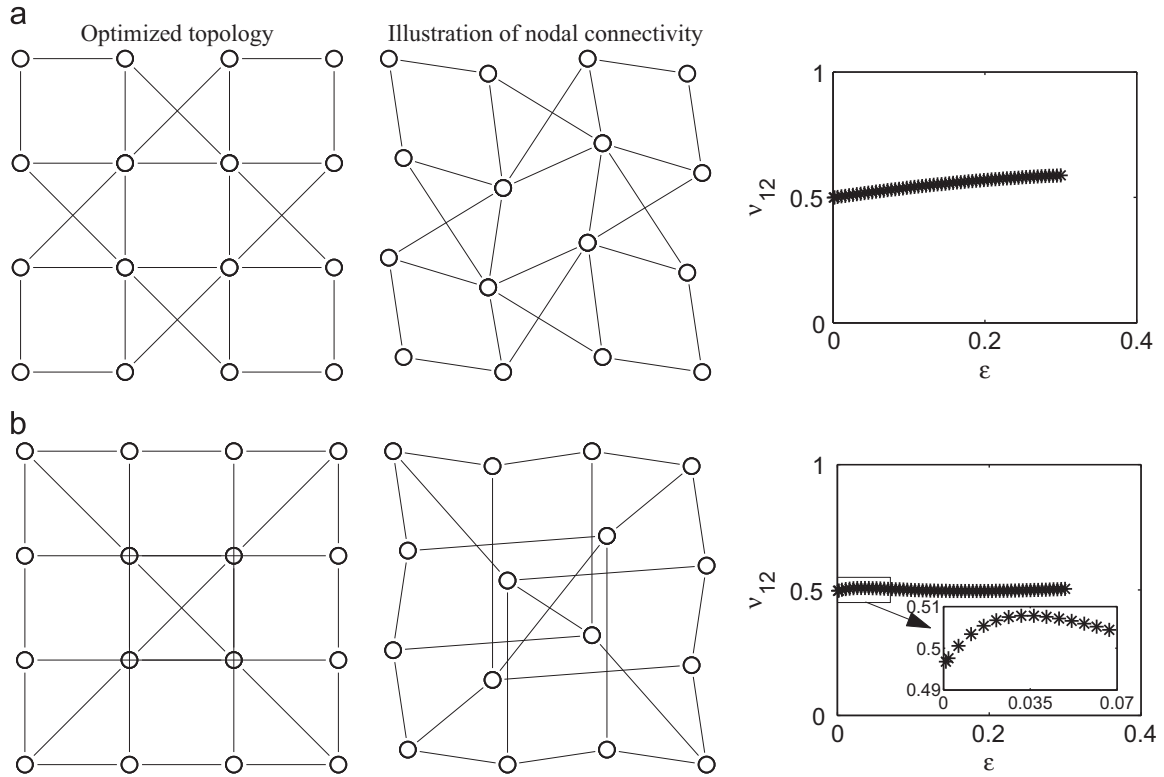
A closer inspection of the geometries of the optimized materials for NPR reveals that the optimized materials bear a resemblance to a certain class of auxetic materials, i.e. chiral honeycombs (Lakes, 1991; Prall and Lakes, 1997; Alderson et al., 2010; Elise and Lantada, 2012). Chiral honeycombs have been numerically and experimentally demonstrated to possess negative Poisson's ratio effect under finite deformation. The asymmetrical optimized material shows similarity to tetrachiral honeycombs (see Fig. 15(a)) and the symmetrical material is similar to the anti-tetrachiral honeycombs in Fig. 15(b). Furthermore, the symmetrical optimized material resembles the topologies of one type of the negative Poisson's material induced by elastic instability (Bertoldi et al., 2010), where pattern transformations lead to unidirectional negative Poisson's ratio behavior of 2D structures when compression is beyond a certain point.

Pertaining to the question of stability, we emphasize that our design methodology does not guarantee macroscopic stability for compressive loading. Numerical simulations with a finite number of unit cells indicate that the asymmetric designs tend to display macroscopic buckling with a prescribed compressive loading of sufficient magnitude, if the transverse displacements are unconstrained. For the symmetric designs the corresponding macrostructures appear to be stable.

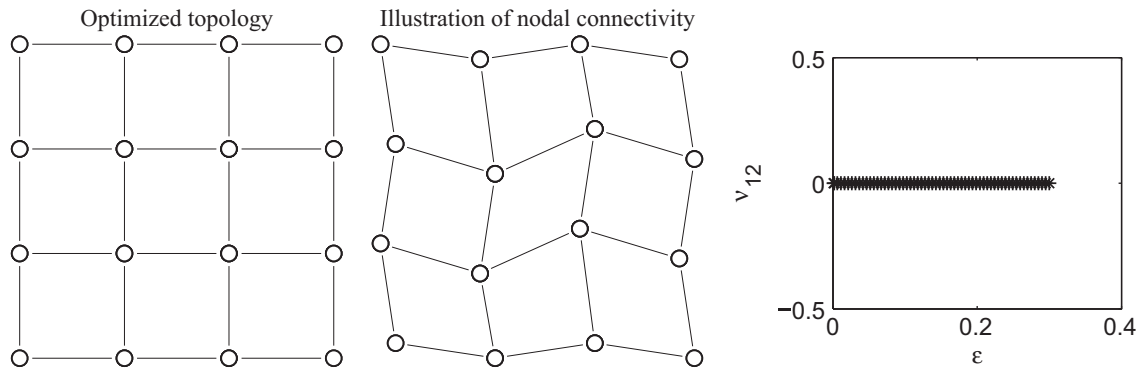
#### 4.4. Robust 2D continuum materials with prescribed Poisson's ratio

It is known that manufacturing errors may severely degrade the optimized properties of materials obtained by topology optimization (Sigmund, 2009). In this section, we firstly investigate the performance of the optimized materials in the previous subsection with respect to certain manufacturing errors. Then we employ a robust optimization formulation to enhance the design robustness of optimized materials with respect to manufacturing errors.

The different design realizations during a manufacturing procedure can be emulated by using different thresholds in Eq. (8), assuming uniformly distributed errors. The performance of the optimized materials are evaluated using 11 different design realizations approximated using 11 equidistant thresholds in the interval of  $\eta \in [0.45, 0.55]$ .



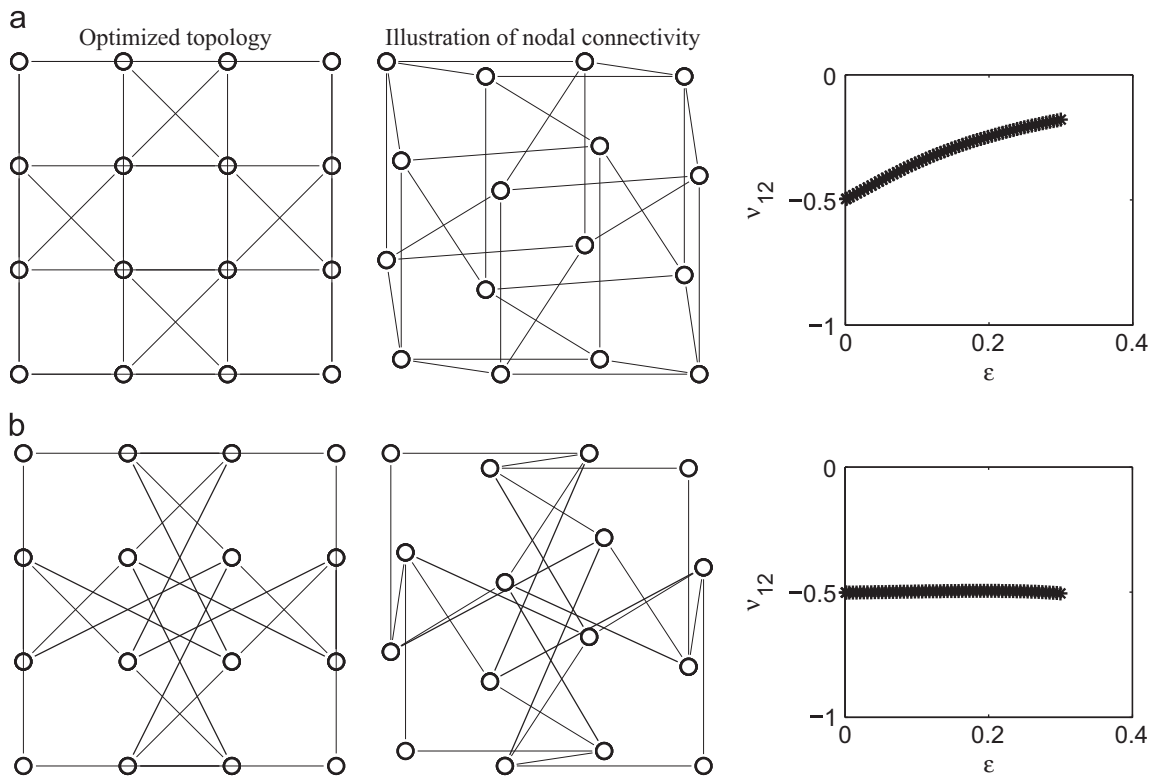
**Fig. 8.** Optimized materials for  $\nu^* = 0.5$  and corresponding performances under finite deformation. (a) Optimized material under small deformation and corresponding Poisson's ratio function under finite deformation. (b) Optimized material under finite deformation and corresponding Poisson's ratio under finite deformation.



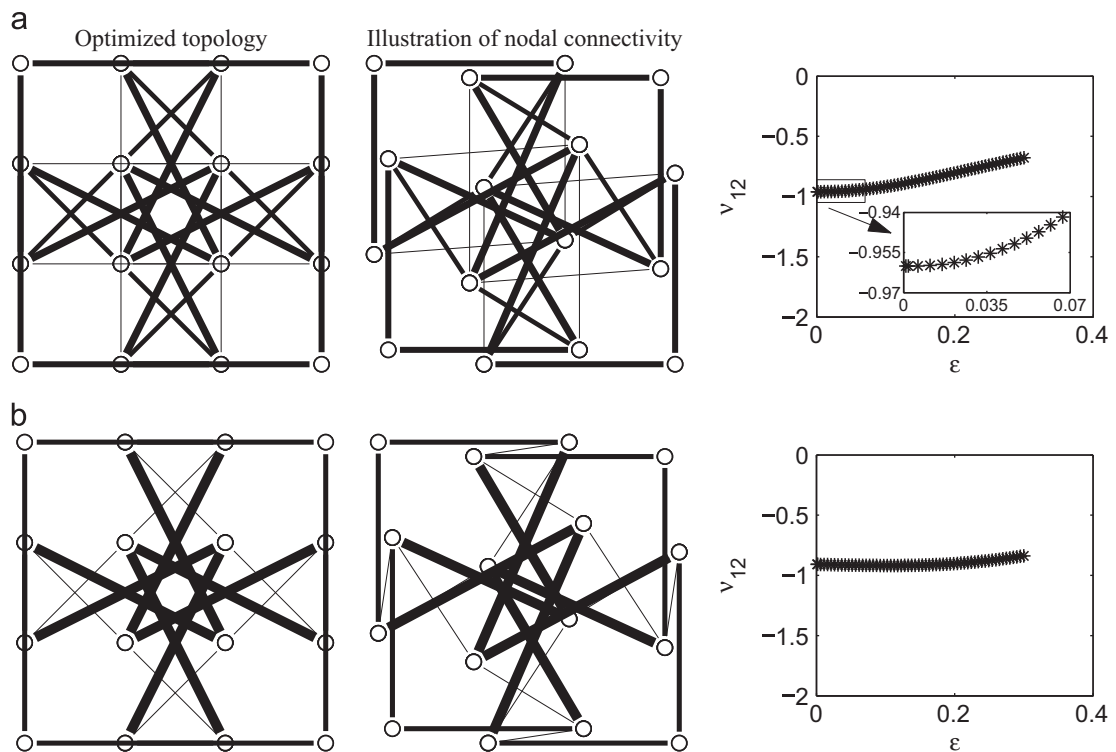
**Fig. 9.** Optimized material for  $\nu^* = 0.0$  and corresponding performances under finite deformation.

Fig. 16 shows the performance of the optimized materials for the target Poisson's ratio of  $\nu^* = -1.0$ . The left panels indicate the manufacturing errors considered, where bold solid lines indicate the contour of the optimized material ( $\eta = 0.50$ ), the dot-dashed lines show the contour of the eroded design realization approximated by  $\eta = 0.55$ , and the dashed lines show the dilated design realization approximated by  $\eta = 0.45$ . The middle and right panels show the performance of different design realizations in terms of  $\nu_{12}$  and  $\nu_{21}$ , where the dots and lines indicate the averaged Poisson's ratio and the corresponding Poisson's ratio range in the target axial strain range for each design realization, respectively.

It is seen from Fig. 16(a) that the averaged Poisson's ratio of the asymmetrical material decreases as the threshold increases, and that the Poisson's ratio variation increases significantly when the optimized material is dilated ( $\eta < 0.50$ ). The performance improvement in the eroded design realizations ( $\eta > 0.50$ ) can be ascribed to the increased unrolling action from dilated design realizations to eroded design realizations. Meanwhile, the performance of the optimized design realization ( $\eta = 0.50$ ) is restricted by the stiffness constraints in both axial directions. It is anticipated that better performance can be achieved by relaxing the stiffness constraints, as indicated by the eroded design realizations. On the other hand, the performance of the symmetrical material in Fig. 16(b) shows that big variations of Poisson's ratio are



**Fig. 10.** Optimized materials for  $\nu^* = -0.5$  and corresponding performances under finite deformation. (a) Optimized material under small deformation and corresponding Poisson's ratio function versus axial strain. (b) Optimized material under finite deformation and corresponding performance.



**Fig. 11.** Optimized materials for  $\nu^* = -1.0$  and corresponding performances under finite deformation. (a) Optimized material under small deformation and corresponding performance. (b) Optimized material under finite deformation and corresponding Poisson's ratio function.

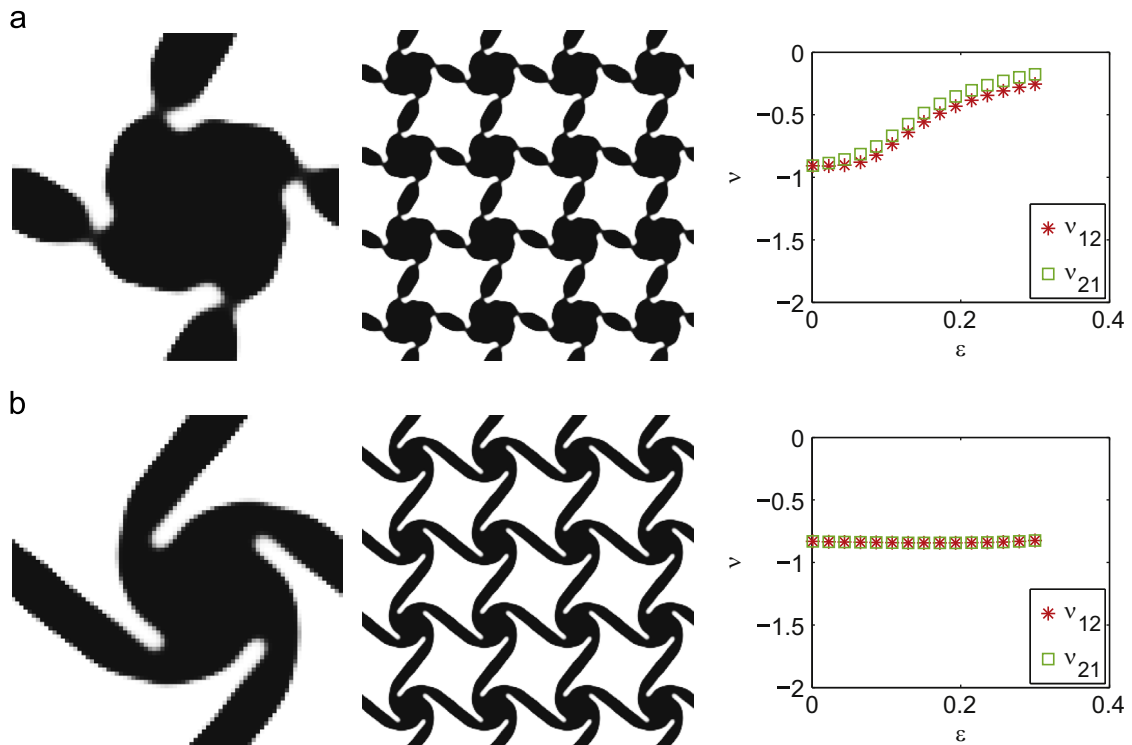


**Fig. 12.** Optimized materials for  $\nu^* = -1.0$  and corresponding performances. (a) Optimized material under small deformation. (b) Optimized material under finite deformation.

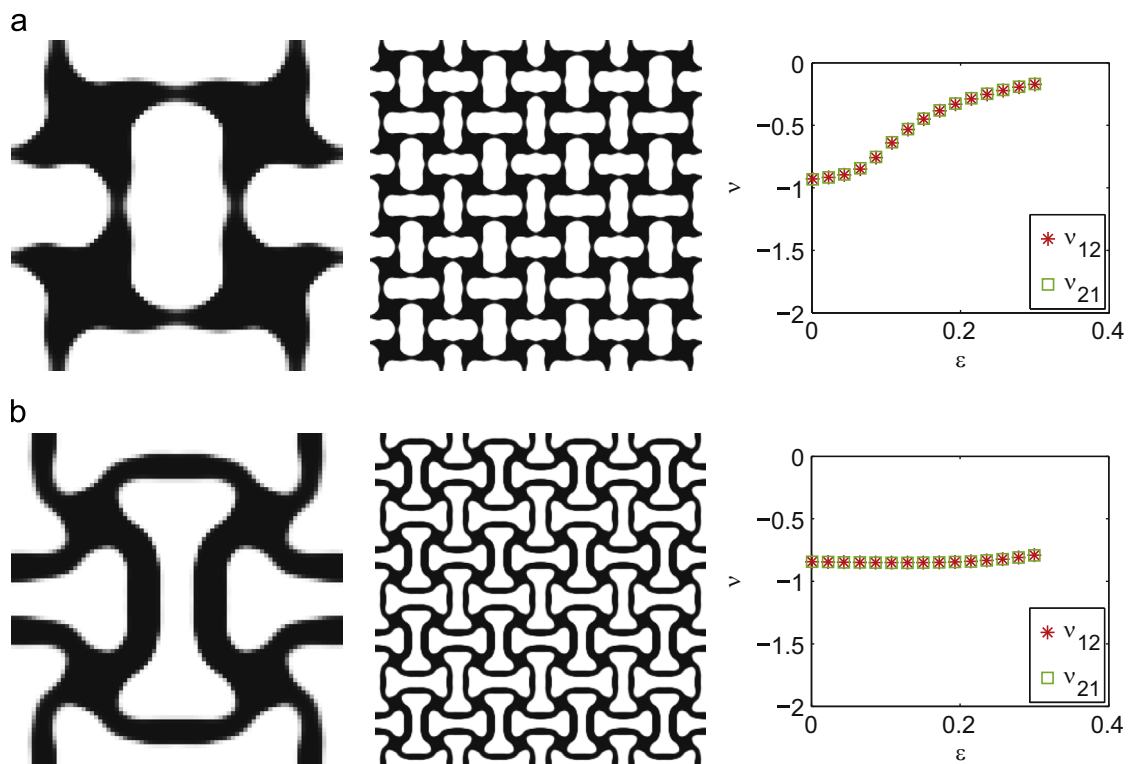


**Fig. 13.** Optimized symmetrical materials for  $\nu^* = -1.0$  and corresponding performances. (a) Optimized material under small deformation. (b) Optimized material under finite deformation.

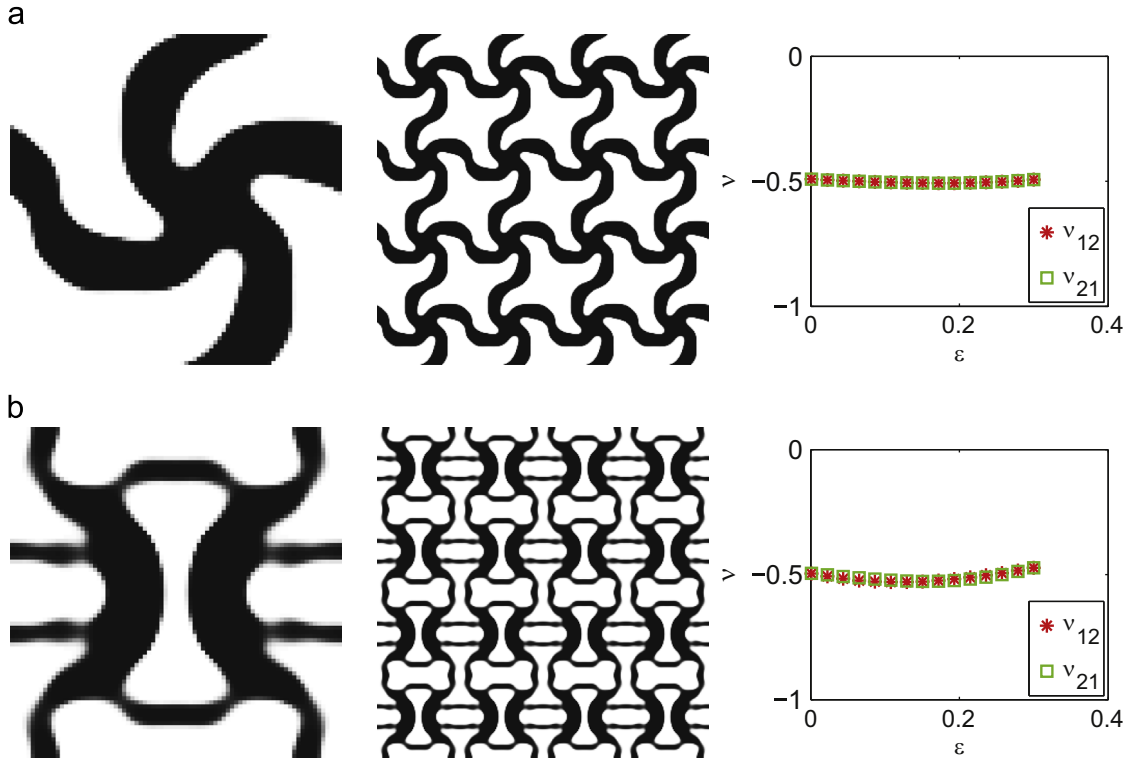


**Fig. 14.** Optimized materials for  $\nu^* = -0.5$  and corresponding performances. (a) Optimized asymmetrical material. (b) Optimized symmetrical material.

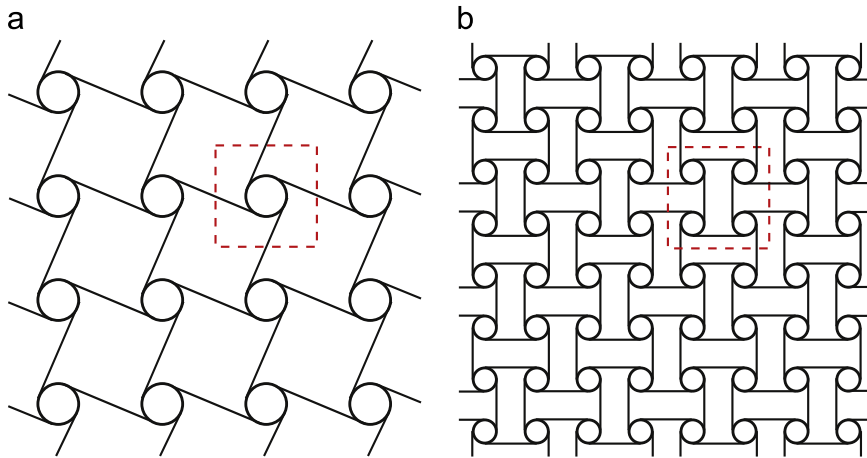


**Fig. 15.** Geometries of auxetic chiral honeycombs with the dashed squares indicating unit cells (Alderson et al., 2010). (a) Tetrachiral honeycombs. (b) Anti tetrachiral honeycombs.

observed in the eroded design realization of  $\eta = 0.55$ . This is caused by the disconnection of parts of the microstructure induced by erosion, as indicated in the left panel in Fig. 16(b).

Fig. 17 shows the performances of the asymmetrical and symmetrical optimized materials for  $\nu^* = -0.5$  under manufacturing errors. It is seen that the asymmetrical material still maintains a small Poisson's ratio variation under different manufacturing errors. Similar to the case of  $\nu^* = -1.0$ , the average Poisson's ratio decreases as the threshold increases, which implies that the eroded design realizations possess better performance than the optimized design realization. The symmetrical material exhibits large Poisson's ratio variation under dilation ( $\eta < 0.50$ ) and large average Poisson's ratio under erosion ( $\eta > 0.50$ ).

This investigation has shown that the optimized materials are relatively sensitive to manufacturing errors, except the asymmetrical material for  $\nu^* = -0.5$ . Hence, it is desirable to enhance the robustness of the designs. In this paper,



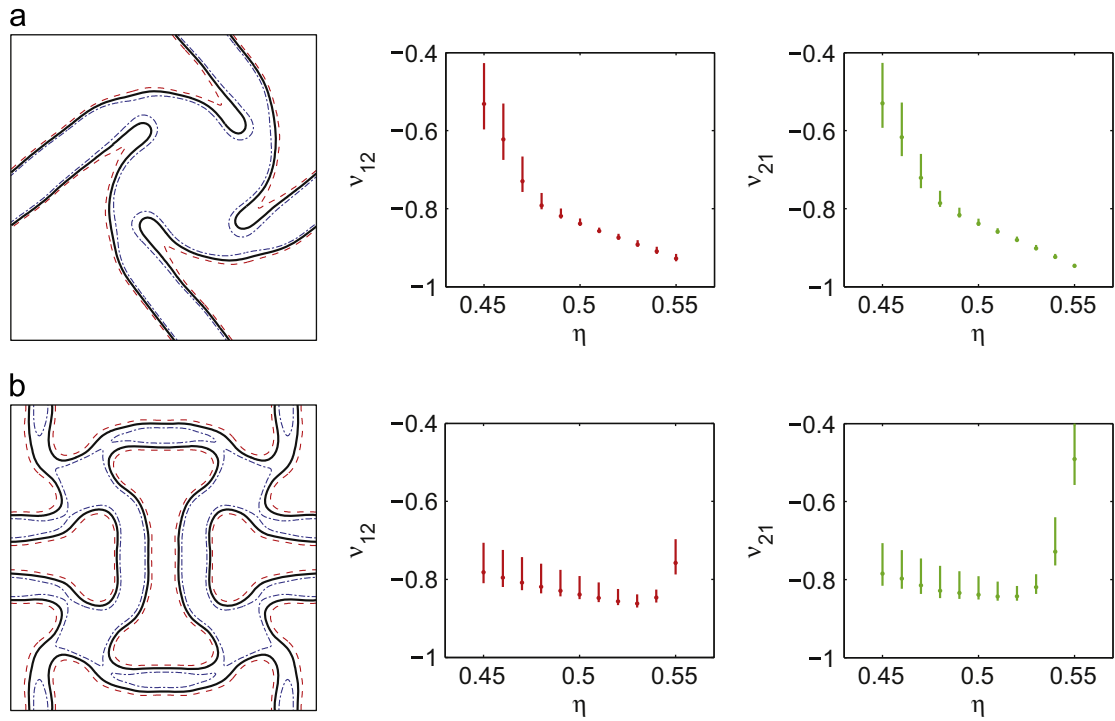


**Fig. 16.** (a) Performance of the asymmetrical material of  $\nu^* = -1.0$  under manufacturing errors. The left panel: contour plots of different design realizations, the optimized design realization  $\eta = 0.50$  in bold solid lines, the eroded design realization of  $\eta = 0.55$  in the dot-dashed lines and the dilated design realization of  $\eta = 0.45$  in the dashed line. The middle panel:  $\nu_{12}$  versus design realizations. The right panel:  $\nu_{21}$  versus design realizations. (b) Performance of the symmetrical material of  $\nu^* = -1.0$  with respect to manufacturing errors.

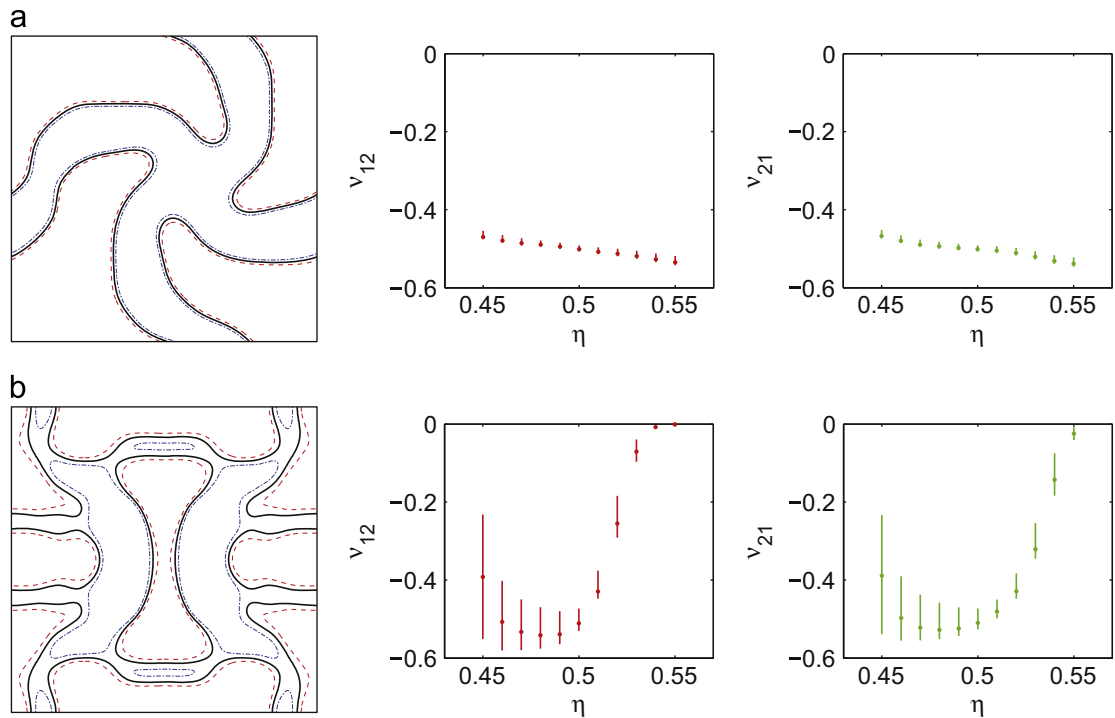


**Fig. 17.** (a) Performance of the asymmetrical optimized material of  $\nu^* = -0.5$  under manufacturing errors. (b) Performance of the symmetrical optimized material of  $\nu^* = -0.5$  under manufacturing errors.

we employ the 3-case robust optimization formulation presented by Wang et al. (2011). The objective is modified to minimize the maximum error between the actual and prescribed Poisson's ratios in the target axial strain range among three different design realizations, i.e. the dilated design ( $\eta_d = 0.45$ ), the optimized design ( $\eta_i = 0.50$ ) and the eroded design ( $\eta_e = 0.55$ ), stated as

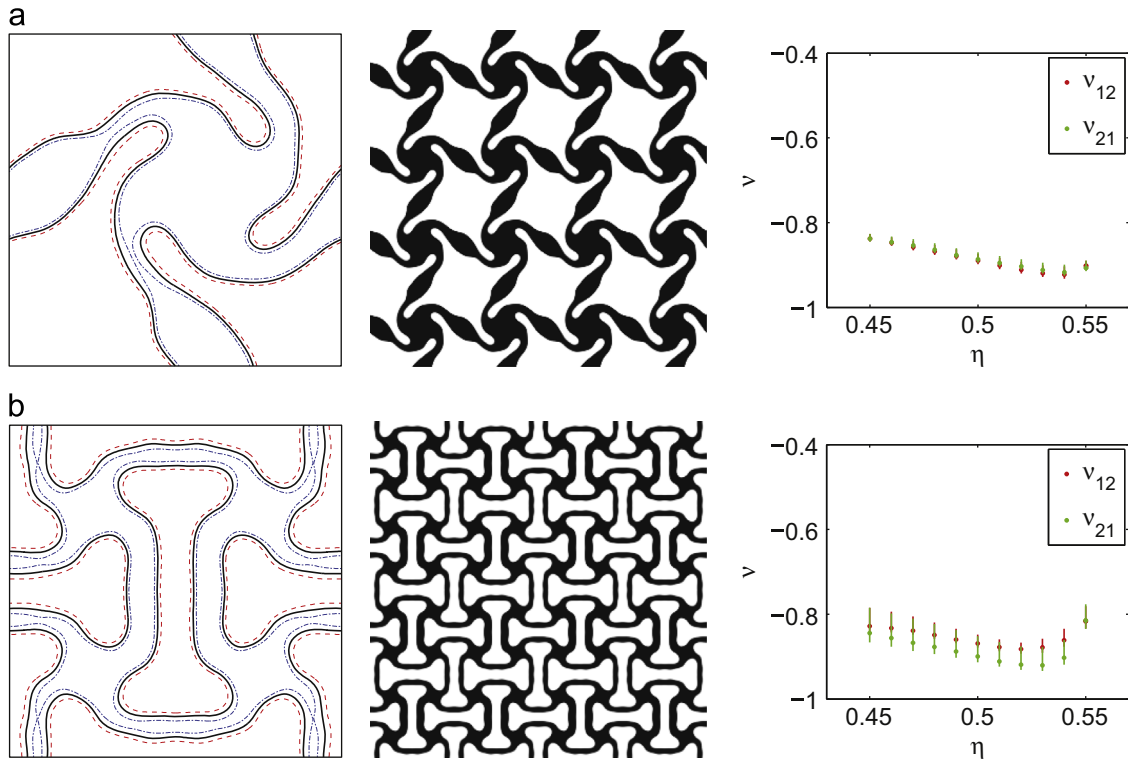
$$\min_{\mathbf{x}} \max_{\eta \in [\eta_d, \eta_i, \eta_e]} \max_{\varepsilon_i} f = (\nu(\eta, \varepsilon_i) - \nu^*)^2 \quad (16)$$

Fig. 18 shows the robust asymmetrical and symmetrical materials for  $\nu^* = -1.0$  and the corresponding performances considering manufacturing errors. The left panels illustrate the manufacturing errors considered in the optimization procedure, the middle panels show the robust optimized materials consisting of  $4 \times 4$  periods of microstructures, and the right panels show the performance of the optimized materials with respect to different manufacturing errors. A comparison with Fig. 16 reveals that the robust optimized materials display a much more robust performance. A variation on the averaged Poisson's ratio can still be observed, however, with the asymmetrical material exhibiting a significantly smaller variation for the different design realizations.

It is observed that the three design realizations show the same topology in both materials, although the eroded symmetrical design exhibits a zero length scale in the solid phase. This implies that minimal length scales on both the void and solid phases are guaranteed in the optimized design realizations (Wang et al., 2011).

Robust optimized materials for  $\nu^* = -0.5$  are shown in Fig. 19. The robust asymmetrical material maintains nearly constant averaged Poisson's ratio and small Poisson's ratio variations under manufacturing errors. The robust symmetrical material shows much better performance compared to the single-case design and Poisson's ratio variation is narrowed down to  $\nu \in [0.4, 0.6]$  in the target axial strain range. However, Poisson's ratio variations of the robust symmetrical material are significantly larger than for the asymmetrical material. As in the case of  $\nu^* = -1.0$ , minimal length scales on both void and solid phases are observed in both optimized design realizations.

As the final examples, Fig. 20(a) and (b) shows robust optimized symmetrical materials for positive Poisson's ratios of  $\nu^* = 0.5$  and  $\nu^* = 1.0$ . In both cases, the eroded design realizations display zero length scale in the solid phase, and identical topologies among different design realizations ensure minimal length scales on both phases. The optimized material for  $\nu^* = 1.0$  exhibits relatively large Poisson's ratio variations compared to the other robust materials.



**Fig. 18.** Robust optimized materials for  $\nu^* = -1.0$ . (a) Asymmetrical optimized material. The left panel: manufacturing errors considered. The middle panel: the optimized design realization. The right panel: the performance of the optimized material under manufacturing errors. (b) Symmetrical optimized material and corresponding performance under manufacturing errors.

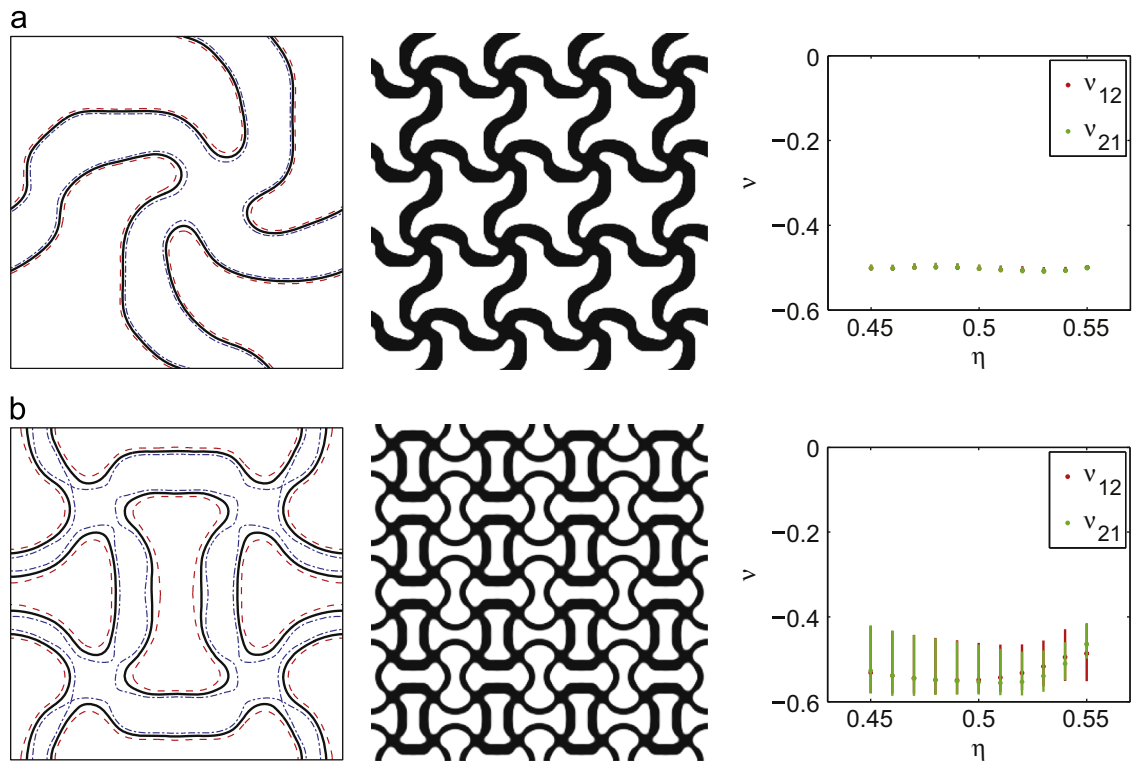


**Fig. 19.** Robust optimized materials for  $\nu^* = -0.5$ . (a) Asymmetrical optimized material and corresponding performance. (b) Symmetrical optimized material and corresponding performance.

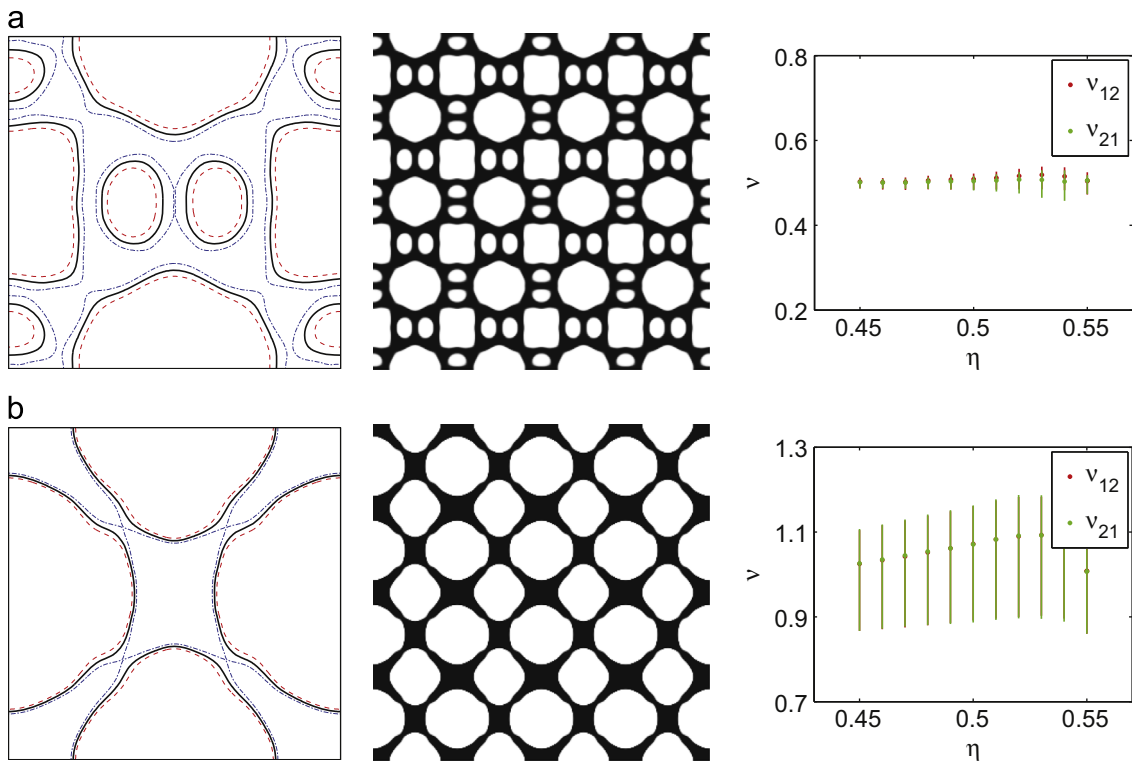


**Fig. 20.** (a) Robust optimized material for  $\nu^* = 1.0$  and corresponding performance. (b) Robust optimized material for  $\nu^* = 0.5$  and corresponding performance.

## 5. Conclusion

In this paper, we study the optimization problem of material design for prescribed nonlinear properties under finite deformation focusing on tensile tests. A numerical model is proposed to characterize material properties for longitudinal and transverse tensile test in terms of stress–strain curves and Poisson's ratio. Optimization problems have been formulated to design materials with prescribed stress–strain curves and with prescribed Poisson's ratio under finite deformation. Both the objectives have been formulated to minimize the errors between actual and prescribed properties in a prescribed axial strain range.

2D truss-based materials have been designed for prescribed stress–strain curves and prescribed Poisson's ratios. The penalty of either long or short bars has been implemented to simplify the optimized material configurations. Numerical results have shown that the optimized materials can achieve e.g. a rubber-like behavior under finite deformation, and that materials can be tailored for different target Poisson's ratios in the axial strain range of  $\epsilon_i \in [0.00, 0.30]$ .

2D continuum materials have been designed for different target Poisson's ratios, positive and negative, in the axial strain range of  $\epsilon_i \in [0.00, 0.30]$ . This includes both symmetric and non-symmetric designs. Furthermore, the performance of the optimized materials has been investigated with respect to manufacturing errors, and the robustness of optimized materials under manufacturing errors has been enhanced using a 3-case robust optimization formulation. Performances of the robust optimized materials have shown that the optimized materials preserve relative good performances in terms of Poisson's ratio under manufacturing errors, and that the asymmetrical materials with NPR exhibit a much more robust performance than the symmetrical ones. Moreover, detailed comparisons have demonstrated that the optimized materials with NPR bear a resemblance to chiral honeycombs and that the symmetrical materials also resemble the topology of the NPR material induced using elastic instability.

The 2D continuum examples are restricted to plane strain conditions, however, the presented method can be directly employed to design 2D continuum material with a plane stress conditions and also 3D continuum materials. Additionally, the material performance in compression may be taken into account as well by extending the considered target axial strain range.

## Acknowledgments

This work was financially supported by an ERC Starting Grant through INNODYN and by Villum Fonden through the NextTop project. The authors thank Dr. Boyan Stefanov Lazarov at the Department of Mechanical Engineering in the Technical University of Denmark for valuable discussions.

## References

- Alderson, A., Alderson, K.L., Attard, D., Evans, K.E., Gatt, R., Grima, J.N., Miller, W., Ravirala, N., Smith, C.W., Zied, K., 2010. Elastic constants of 3-, 4- and 6-connected chiral and anti-chiral honeycombs subject to uniaxial in-plane loading. *Compos. Sci. Technol.* 70 (7), 1042–1048.
- Alderson, K.L., Evans, K.E., 1992. The fabrication of microporous polyethylene having a negative Poisson's ratio. *Polymer* 33 (20), 4435–4438.
- Alderson, K.L., Fitzgerald, A., Evans, K.E., 2000. The strain dependent indentation resilience of auxetic microporous polyethylene. *J. Mater. Sci.* 35 (16), 4039–4047.
- Alderson, K.L., Pickles, A.P., Neale, P.J., Evans, K.E., 1994. Auxetic polyethylene: the effect of a negative Poisson's ratio on hardness. *Acta Metall. Mater.* 42 (7), 2261–2266.
- Andreassen, C.S., Andreassen, E., Jensen, J.S., Sigmund, O., 2014. On the realization of the bulk modulus bounds for two phase viscoelastic composites. *J. Mech. Phys. Solids* 63, 228–241.
- Andreassen, E., Lazarov, B.S., Sigmund, O., 2014. Design of manufacturable 3D extremal elastic microstructure. *Mech. Mater.* 69, 1–10.
- Bendsøe, M.P., Kikuchi, N., 1988. Generating optimal topologies in structural design using a homogenization method. *Comput. Methods Appl. Mech. Eng.* 71 (2), 197–224.
- Bendsøe, M.P., Sigmund, O., 1999. Material interpolation schemes in topology optimization. *Arch. Appl. Mech.* 69 (9–10), 635–654.
- Bendsøe, M.P., Sigmund, O., 2003. *Topology Optimization: Theory, Methods and Applications*. Springer, Berlin.
- Bertoldi, K., Reis, P.M., Willshaw, S., Mullin, T., 2010. Negative Poisson's ratio behavior induced by an elastic instability. *Adv. Mater.* 22 (3), 361–366.
- Bourdin, B., 2001. Filters in topology optimization. *Int. J. Numer. Methods Eng.* 55, 2143–2158.
- Bruns, T.E., Tortorelli, D.A., 2001. Topology optimization of non-linear elastic structures and compliant mechanisms. *Comput. Methods Appl. Mech. Eng.* 190 (26–27), 3443–3459.
- Bruns, T.E., Tortorelli, D.A., 2003. An element removal and reintroduction strategy for the topology optimization of structures and compliant mechanisms. *Int. J. Numer. Methods Eng.* 57 (10), 1413–1430.
- Buhl, T., Pedersen, C.B.W., Sigmund, O., 2000. Stiffness design of geometrically nonlinear structures using topology optimization. *Struct. Multidiscip. Optim.* 19 (2), 93–104.
- Chekkal, I., Bianchi, M., Remillat, C., Becot, F.X., Jaouen, L., Scarpa, F., 2010. Vibro-acoustic properties of auxetic open cell foam: model and experimental results. *Acta Acust. United Acust.* 96 (2), 266–274.
- Chen, C.P., Lakes, R.S., 1996. Micromechanical analysis of dynamic behavior of conventional and negative Poisson's ratio foams. *J. Eng. Mater. Technol.* 118 (3), 285–288.
- Choi, J.B., Lakes, R.S., 1996. Fracture toughness of re-entrant foam materials with a negative Poisson's ratio: experiment and analysis. *Int. J. Fract.* 80 (1), 73–83.
- Clement, A., Soize, C., Yvonnet, J., 2012. Computational nonlinear stochastic homogenization using a nonconcurrent multiscale approach for hyperelastic heterogeneous microstructures analysis. *Int. J. Numer. Methods Eng.* 91 (8), 799–824.
- Cox, S.J., Dobson, D.C., 1999. Maximizing band gaps in two-dimensional photonic crystals. *SIAM J. Appl. Math.* 59, 2108–2120.
- Diaz, A.R., Sigmund, O., 2010. A topology optimization method for design of negative permeability metamaterials. *Struct. Multidiscip. Optim.* 41 (March (2)), 163–177.

- Elipse, J.C.A., Lantada, A.D., 2012. Comparative study of auxetic geometries by means of computer-aided design and engineering. *Smart Mater. Struct.* 21 (10), 105004.
- Evans, K.E., 1991. Auxetic polymers: a new range of materials. *Endeavour* 15 (4), 170–174.
- Evans, K.E., Donoghue, J.P., Alderson, K.L., 2004. The design, matching and manufacture of auxetic carbon fibre laminates. *J. Compos. Mater.* 38 (2), 95–106.
- Haber, R.B., Jog, C.S., Bendsøe, M.P., 1996. A new approach to variable-topology shape design using a constraint on perimeter. *Struct. Optim.* 11 (1), 1–12.
- Hassani, B., Hinton, E., 1998a. A review of homogenization and topology optimization. I. Homogenization theory for media with periodic structure. *Comput. Struct.* 69 (6), 707–717.
- Hassani, B., Hinton, E., 1998b. A review of homogenization and topology optimization. II. Analytical and numerical solution of homogenization equations. *Comput. Struct.* 69 (6), 719–738.
- Hassani, B., Hinton, E., 1998c. A review of homogenization and topology optimization. III. Topology optimization using optimality criteria. *Comput. Struct.* 69 (6), 739–756.
- Hill, R., 1972. On constitutive macro-variables for heterogeneous solids at finite strain. *Proc. R. Soc. Lond. A. Math. Phys. Sci.* 326 (1565), 131–147.
- Klarbring, A., Stromberg, N., 2013. Topology optimization of hyperelastic bodies including non-zero prescribed displacements. *Struct. Multidiscip. Optim.* 47 (1), 37–48.
- Lakes, R., 1987. Foam structures with a negative Poisson's ratio. *Science* 235 (4792), 1038–1040.
- Lakes, R., 1991. Deformation mechanisms in negative Poisson's ratio materials: structural aspects. *J. Mater. Sci.* 26 (9), 2287–2292.
- Lakes, R., 1993. Advances in negative Poisson's ratio materials. *Adv. Mater.* 5 (4), 293–296.
- Lakes, R.S., Witt, R., 2002. Making and characterizing negative Poisson's ratio materials. *Int. J. Mech. Eng. Educ.* 30 (1), 50–58.
- Lamari, H., Ammar, A., Cartraud, P., Legrain, G., Chinesta, F., Jacquemin, F., 2010. Routes for efficient computational homogenization of nonlinear materials using the proper generalized decompositions. *Arch. Comput. Methods Eng.* 17 (4), 373–391.
- Larsen, U.D., Sigmund, O., Bouwstra, S., 1997. Design and fabrication of compliant micromechanisms and structures with negative Poisson's ratio. *J. Microelectromech. Syst.* 6 (2), 99–106.
- Liu, Q., 2006. Literature Review: Materials with Negative Poisson's Ratios and Potential Applications to Aerospace and Defence. Technical Report.
- Miehe, C., 2003. Computational micro-to-macro transitions for discretized micro-structures of heterogeneous materials at finite strains based on the minimization of averaged incremental energy. *Comput. Methods Appl. Mech. Eng.* 192 (5), 559–591.
- Milton, G.W., 2013. Complete characterization of the macroscopic deformations of periodic unimode metamaterials of rigid bars and pivots. *J. Mech. Phys. Solids* 61 (7), 1543–1560.
- Nakshatrala, P., Tortorelli, D., Nakshatrala, K., 2013. Nonlinear structural design using multiscale topology optimization. Part I. Static formulation. *Comput. Methods Appl. Mech. Eng.* 261–262, 167–176.
- Pedersen, C.B.W., Buhl, T., Sigmund, O., 2001. Topology synthesis of large-displacement compliant mechanisms. *Int. J. Numer. Methods Eng.* 50 (12), 2683–2705.
- Ponte Castañeda, P., 1991. The effective mechanical properties of nonlinear isotropic composites. *J. Mech. Phys. Solids* 39 (1), 45–71.
- Ponte Castañeda, P., Zaidman, M., 1996. The finite deformation of nonlinear composite materials. I. Instantaneous constitutive relations. *Int. J. Solids Struct.* 33 (9), 1271–1286.
- Prall, D., Lakes, R.S., 1997. Properties of a chiral honeycomb with a Poisson's ratio of  $-1$ . *Int. J. Mech. Sci.* 39 (3), 305–314.
- Safari, A., 1994. Development of piezoelectric composites for transducers. *J. Phys. III* 4 (7), 1129–1149.
- Scarpa, F., Yates, J.R., Ciffo, L.G., Patsias, S., 2002. Dynamic crushing of auxetic open-cell polyurethane foam. *Proc. Inst. Mech. Eng. Part C: J. Mech. Eng. Sci.* 216 (12), 1153–1156.
- Scarpa, F., Smith, F.C., 2004. Passive and MR fluid-coated auxetic PU foam – mechanical, acoustic, and electromagnetic properties. *J. Intell. Mater. Syst. Struct.* 15 (12), 973–979.
- Shvets, G., Urzhumov, Y.A., 2005. Electric and magnetic properties of sub-wavelength plasmonic crystals. *J. Opt. A—Pure Appl. Opt.* 7 (2), S23–S31.
- Sigmund, O., 1994. Materials with prescribed constitutive parameters: an inverse homogenization problem. *Int. J. Solids Struct.* 31 (17), 2313–2329.
- Sigmund, O., 1995. Tailoring materials with prescribed elastic properties. *Mech. Mater.* 20 (4), 351–368.
- Sigmund, O., 2007. Morphology-based black and white filters for topology optimization. *Struct. Multidiscip. Optim.* 33 (4–5), 401–424.
- Sigmund, O., 2009. Manufacturing tolerant topology optimization. *Acta Mech. Sin.* 25, 227–239.
- Sigmund, O., Jensen, J.S., 2003. Systematic design of phononic band-gap materials and structures by topology optimization. *Philos. Trans. R. Soc. Lond. Ser. A—Math. Phys. Eng. Sci.* 361 (1806), 1001–1019.
- Sigmund, O., Torquato, S., 1997. Design of materials with extreme thermal expansion using a three-phase topology optimization method. *J. Mech. Phys. Solids* 45 (6), 1037–1067.
- Sigmund, O., Torquato, S., Aksay, I.A., 1998. On the design of 1–3 piezocomposites using topology optimization. *J. Mater. Res.* 13 (4), 1038–1048.
- Silva, E.C.N., Fonseca, J.S.O., Kikuchi, N., 1998. Optimal design of periodic piezocomposites. *Comput. Methods Appl. Mech. Eng.* 159 (1–2), 49–77.
- Smith, C.W., Wootton, R.J., Evans, K.E., 1999. Interpretation of experimental data for Poisson's ratio of highly nonlinear materials. *Exp. Mech.* 39 (4), 356–362.
- Svanberg, K., 1987. The method of moving asymptotes—a new method for structural optimization. *Int. J. Numer. Methods Eng.* 24 (2), 359–373.
- Schwerdtfeger, J., Schury, F., Stingl, M., Wein, F., Singer, R.F., Koerner, C., 2012. Mechanical characterisation of a periodic auxetic structure produced by SEBM. *Phys. Status Solidi B* 249 (7), 1347–1352.
- Talbot, D., Willis, J., 1985. Variational principles for inhomogeneous non-linear media. *IMA J. Appl. Math.* 35 (1), 39–54.
- Wang, F., Lazarov, B.S., Sigmund, O., 2011. On projection methods, convergence and robust formulations in topology optimization. *Struct. Multidiscip. Optim.* 43 (6), 767–784.
- Wang, F., Lazarov, B.S., Sigmund, O., Jensen, J.S., 2014. Interpolation scheme for fictitious domain techniques and topology optimization of finite strain elastic problems. *Comput. Methods Appl. Mech. Eng.* 276, 453–472.
- Xu, S.L., Cai, Y.W., Cheng, G.D., 2010. Volume preserving nonlinear density filter based on heaviside functions. *Struct. Multidiscip. Optim.* 41 (April (4)), 495–505.
- Yi, Y.-M., Park, S.-H., Youn, S.-K., 2000. Design of microstructures of viscoelastic composites for optimal damping characteristics. *Int. J. Solids Struct.* 37 (35), 4791–4810.
- Yoon, G.H., Kim, Y.Y., 2005. The element connectivity parameterization formulation for the topology design optimization of multiphysics systems. *Int. J. Numer. Methods Eng.* 64 (12), 1649–1677.
- Yvonnet, J., Gonzalez, D., He, Q.C., 2009. Numerically explicit potentials for the homogenization of nonlinear elastic heterogeneous materials. *Comput. Methods Appl. Mech. Eng.* 198 (33–36), 2723–2737.
- Yvonnet, J., He, Q.-C., 2010. A non-concurrent multiscale method for computing the response of hyperelastic heterogeneous structures. *Eur. J. Comput. Mech.* 19 (1–3), 105–116.
- Zienkiewicz, O.C., Taylor, R.L., 2005. *The Finite Element Method for Solid and Structural Mechanics*. Elsevier Butterworth-Heinemann, Amsterdam, Boston.